Commutation errors in PITM simulation

Bruno Chaouat*
ONERA , 92322 Châtillon, France

Abstract

We examine the effect of variable filter width in the partially integrated transport modeling (PITM) method in the framework of second moment closure (SMC) and the commutation errors arising from the non-commutativity of the filtering process with temporal or spatial derivatives. We propose a method to account for this effect in PITM numerical simulations. In particular, we model the commutation terms in a practical way to get tractable Navier-Stokes and turbulence equations. We apply a discrete approximation to the top hat filter to compute the commutation terms for the velocities and turbulent stresses by means of a superfilter width. A special attention is devoted to the treatment of the turbulent stresses. Moreover, a physical interpretation of the commutation terms is given in the spectral space involving the flux of energy transfer of the spectrum. For illustration purpose, we perform numerical simulations of the fully developed turbulent channel flow on several grids including a sudden grid step increase in the grid-size in the streamwise direction that is akin to grid discontinuities. The commutation errors are then distributed in a small delimited region of the field. As a result, we found that the impact of the commutation terms on the PITM solution remains moderate even if the grid-size variation is increasing up to 400 % in the streamwise direction but the accounting for the commutation errors has however a slight beneficial effect on the solution by improving the flow prediction.

1 Introduction

Large eddy simulation (LES) which consists in modeling the more universal scales while the large scales motions are explicitly computed is a promising tool (Lesieur and Métais, 1996) that is complementary to Reynolds averaged Navier-Stokes equations (RANS) that is still often used in industries for predicting steady flows (Chaouat, 2006; Gatski et al., 2007; Jakirlic et Maduta, 2015). LES has been especially developed in the past two decades for simulating unsteady flows with emphasis on fundamental aspects including the flow structures, the statistical post analysis based on two-point correlation and spectral properties. This method is costly in term of computational resources for industrial applications involving turbulent flows at high Reynolds numbers, even with the increase of super-computer power. This is the reason which has led researchers to develop hybrid

*Senior Scientist, Department of Computational Fluid Dynamics. E-mail address: Bruno.Chaouat@onera.fr

RANS-LES methods that combine advantages of both RANS and LES methods. These methods were referenced recently by different authors (Frölhlich and Von Terzi, 2008; Argyropoulos and Markatos, 2015; Chaouat, 2017a). Among these hybrid RANS-LES methods, we focus interest in the partially integrated transport modeling (PITM) method developed by Schiestel and Dejoan (2005) using two equation subfilter scale viscosity models and by Chaouat and Schiestel (2005) for the extension to stress transport subfilter scale models in the framework of second moment closure (SMC) (Schiestel, 2008, Hanjalic and Launder, 2011). The modeling of the dissipation-rate by its transport equation using spectral splitting techniques and partial integration in the spectral space is the cornerstone of this method (Schiestel and Dejoan, 2005; Chaouat and Schiestel, 2005). This one has been proposed for simulating non-equilibrium unsteady flows on relatively coarse grids with seamless coupling between the RANS and LES regions considering that the cutoff wave number can be placed everywhere in the spectrum and in particular before the inertial zone within the energy spectrum as far as the grid-size is however sufficient to describe correctly the mean flow. In this case, an appreciable part of subfilter energy is modeled by means of transport equations of the turbulent field variables. Overall, the PITM method has proved to be a promising route for various applications encountered in aeronautics and space (Chaouat and Schiestel, 2005; Befeno and Schiestel, 2007; Chaouat, 2012; Chaouat and Schiestel, 2013; Stoellinger et al., 2015; Kenjeres et al., 2015; Chaouat, 2017b). Generally speaking, subfilter models derived from the PITM method vary continuously from RANS to LES with respect to a parameter formed from the ratio of the turbulence length-scale L_e to the grid-size Δ. This method was initially developed for constant filter width or at least filter width slowly varying in time and space. However, certain applications require to perform PITM simulations of temporally or spatially evolving turbulent flows on moving meshes or distorted meshes. In addition, for computational strategies in complex geometries, the grids can be suddenly coarsened or refined to optimize the resolution capacity of the grid with a given number of points. As a consequence, numerical errors caused by the change of the grid-size may propagate into the flow leading to the possibility of unphysical results.

In framework of LES, and more precisely, eddy viscosity models, several authors, Ghosal and Moin (1995), van der Bos and Geurts (2004), Geurts and Holm (2006), Fureby and Tabor (1997), investigated the effect of a varying grid-size for several types of flow and especially the commutation errors arising from the non-commutativity of the filtering process with temporal or spatial derivatives. Vasilyev et al. (1998), van der Bos and Geurts (2005) analyzed the magnitude of the commutation terms assuming that the flow variables are sufficiently smooth to be developed in Taylor series expansion in space. Van der Bos and Geurts (2005) validated their result using *a priori* tests based on DNS data in turbulent mixing layers. More recently, in framework of hybrid zonal RANS-LES methods, Hamba (2011) studied the filtered Navier-Stokes equations with a special attention paid to the interface treatment. As a result, Hamba indicated that zonal hybrid RANS-LES simulations neglecting the commutation terms underpredict the velocity fluctuations in the interface region leading to the velocity mismatch in channel flow.

In the present work, we will investigate the effect of a varying filter width on PITM flow solution in continuous hybrid non-zonal RANS-LES simulations using second moment closure. As a starting point, we will examine the equations of the subfilter scale stress model and especially the commutation errors arising from the non-commutativity of the filtering process with temporal or spatial derivatives, and we will propose a method to account for this effect in numerical simulations. Special attention will be paid to the treatment of the turbulent stresses. Then, we will give a physical interpretation of the commutation terms in the spectral space. We will check the consistency of the turbulence model and address the issue of realizability in second moment closure modeling accounting for the commutation terms. For illustration purpose, we will perform then numerical simulations of the well known fully developed turbulent channel flow on several grids where the commutation errors are concentrated in a given field region due to a sudden grid step increase in the grid-size in the streamwise direction. With the aim to investigate this effect without any contamination and potential source of errors, we will develop a specific numerical tool of generation of fully developed turbulence. We will especially examine the mean velocity profile, the subfilter, resolved and total turbulent stresses including the sharing out of turbulent energy between the modeled and resolved scales, and the evolution of the turbulence length-scale when passing from uniform grids to coarse grids. The PITM simulations will be compared with the direct numerical simulation performed at the friction Reynolds number $R_\tau = 395$ (Moser et al., 1999).

2 Commutation terms

Turbulent flow of a viscous incompressible flow is considered. In RANS methodology, each variable ϕ can be decomposed into a statistical part $\langle\phi\rangle$ and a fluctuating part ϕ' such as $\phi = \langle\phi\rangle + \phi'$ whereas in large eddy simulation, the variable ϕ is decomposed into a large scale (or resolved part) $\bar{\phi}$ and a subfilter-scale fluctuating part $\phi^>$ or modeled part such that $\phi = \bar{\phi} + \phi^>$. The instantaneous fluctuation ϕ' contains in fact the large scale fluctuating part $\phi^<$ and the small scale fluctuating part $\phi^>$ such that $\phi' = \phi^< + \phi^>$. The filtered variable $\bar{\phi}$ is defined by the filtering operation as the convolution with a filter G in space $\overline{\phi} = G * \phi$ that leads to the computation of a variable convolution integral

$$\bar{\phi}(\boldsymbol{x}, t) = \int_\Omega G\left[\boldsymbol{x} - \boldsymbol{\xi}, \Delta(\boldsymbol{x}, t)\right] \phi(\boldsymbol{\xi}, t) d\boldsymbol{\xi} \tag{1}$$

where in this expression, Δ denotes the filter-width that varies in time and space and Ω denotes the infinite flow domain. The filter function G satisfies the normalization condition

$$\int_\Omega G\left[\boldsymbol{x} - \boldsymbol{\xi}, \Delta(\boldsymbol{x}, t)\right] d\boldsymbol{\xi} = 1 \tag{2}$$

As known, the properties of the filtering process are different from those of the statistical averaging process. In particular, $\bar{\bar{\phi}} \neq \bar{\phi}$, $\langle\phi^<\rangle = -\langle\phi^>\rangle \neq 0$. As a result of interest, note also that $\langle\bar{\phi}\rangle = \langle\phi\rangle - \langle\phi^>\rangle \neq \langle\phi\rangle$ so that there is no direct connection between the averaged field in a statistical sense and the filtered field in LES. But, all these difficulties disappear in an homogeneous turbulent field. So that the instantaneous variable ϕ can be then rewritten very clearly as the sum of a mean statistical part $\langle\phi\rangle$, a large scale fluctuating part $\phi^< = \bar{\phi} - \langle\phi\rangle$, and a small scale fluctuating part $\phi^>$. In the general case, the key concept is to consider the tangent homogeneous anisotropic turbulence field at the physical space location $\boldsymbol{X}$ within the nonhomogeneous field (Chaouat and Schiestel, 2007; Chaouat and Schiestel, 2009) implying that the variation of the mean velocities u_k is accounted for by the use of Taylor series expansion in space limited to the linear terms such that $\langle u_k\rangle(X_m+\xi_m) = \langle u_k\rangle(X_m) + \Lambda_{kj}\xi_j$ where Λ_{kj} is a constant tensor, we recover the interesting property establishing the link between the RANS and LES methodologies (Chaouat and Schiestel, 2007)

$$\overline{\langle u_k\rangle}(X_m+\xi_m) = \overline{\langle u_k\rangle(X_m) + \Lambda_{kj}\xi_j} = \langle u_k\rangle(X_m) \tag{3}$$

because the convolution of $\Lambda_{kj}\xi_j$ with G reduces to zero, G being an even function. Strictly speaking, hence, as a consequence of equation (3), we now get the property $\overline{\langle\phi\rangle} = \langle\bar{\phi}\rangle = \langle\phi\rangle$ if we work in the tangent homogeneous space. In general practice however, if the tangent homogeneous space approximation is not used, one can assume that $\langle\bar{\phi}\rangle \approx \langle\phi\rangle$ only if the variation of the flow velocities over the filter width is not too large. Due to the fact that the filtering operation does not commute with the space derivative, a commutation term appears in the derivative in space $\partial\bar{\phi}/\partial x_i$ as (Iovieno and Tordella, 2003; Chaouat and Schiestel, 2013)

$$\frac{\partial\bar{\phi}}{\partial x_i}(\boldsymbol{x},t) = \overline{\frac{\partial\phi}{\partial x_i}}(\boldsymbol{x},t) + \frac{\partial\Delta}{\partial x_i}\frac{\partial\bar{\phi}}{\partial\Delta}(\boldsymbol{x},t) \tag{4}$$

and equivalently , if transposing equation (4) in time for the derivative $\partial\bar{\phi}/\partial t$

$$\frac{\partial\bar{\phi}}{\partial t}(\boldsymbol{x},t) = \overline{\frac{\partial\phi}{\partial t}}(\boldsymbol{x},t) + \frac{\partial\Delta}{\partial t}\frac{\partial\bar{\phi}}{\partial\Delta}(\boldsymbol{x},t) \tag{5}$$

The commutation errors in space and time are defined, respectively, by

$$\mathcal{C}_{x_i}(\phi) = \overline{\frac{\partial\phi}{\partial x_i}}(\boldsymbol{x},t) - \frac{\partial\bar{\phi}}{\partial x_i}(\boldsymbol{x},t) = -\frac{\partial\Delta}{\partial x_i}\frac{\partial\bar{\phi}}{\partial\Delta}(\boldsymbol{x},t) \tag{6}$$

$$\mathcal{C}_{t}(\phi) = \overline{\frac{\partial\phi}{\partial t}}(\boldsymbol{x},t) - \frac{\partial\bar{\phi}}{\partial t}(\boldsymbol{x},t) = -\frac{\partial\Delta}{\partial t}\frac{\partial\bar{\phi}}{\partial\Delta}(\boldsymbol{x},t) \tag{7}$$

The issue to address first is to compute the material derivative of any variable ϕ of the flow

$$\frac{d\phi}{dt} = \frac{\partial\phi}{\partial t} + \frac{\partial(u_j\phi)}{\partial x_j} \tag{8}$$

Applying the filtering operation on equation (8) yields

$$\overline{\frac{d\phi}{dt}} = \overline{\frac{\partial\phi}{\partial t}} + \overline{\frac{\partial(u_j\phi)}{\partial x_j}} \tag{9}$$

Then, if using equation (4) for the derivative in space and the corresponding equation (5) for the derivative in time, we get

$$\overline{\frac{d\phi}{dt}} = \frac{\partial\bar{\phi}}{\partial t} - \frac{\partial\Delta}{\partial t}\frac{\partial\bar{\phi}}{\partial\Delta} + \frac{\partial(\overline{u_j\phi})}{\partial x_j} - \frac{\partial\Delta}{\partial x_j}\frac{\partial(\overline{u_j\phi})}{\partial\Delta} \tag{10}$$

The correlation $\overline{u_j\phi}$ appearing in equation (10) can be developed in a more explicit form as

$$\overline{u_j\phi} = \bar{u}_j\bar{\phi} + [\overline{u_j\phi} - \bar{u}_j\bar{\phi}] = \bar{u}_j\bar{\phi} + \tau(u_j,\phi) \tag{11}$$

where $\tau(u_j,\phi)$ is a function defined as $\tau(u_j,\phi) = \overline{u_j\phi} - \bar{u}_j\bar{\phi}$. So that equation (10) becomes

$$\overline{\frac{d\phi}{dt}} = \frac{\partial\bar{\phi}}{\partial t} + \frac{\partial(\bar{u}_j\bar{\phi})}{\partial x_j} + \frac{\partial\tau(u_j,\phi)}{\partial x_j} - \beta_T(\phi) \tag{12}$$

where $\beta_T(\phi) = \beta_t(\phi) + \beta_{x_j}(u_j\phi)$ with

$$\beta_t(\phi) = \frac{\partial\Delta}{\partial t}\frac{\partial\bar{\phi}}{\partial\Delta} \tag{13}$$

$$\beta_{x_j}(u_j\phi) = \frac{\partial\Delta}{\partial x_j}\frac{\partial}{\partial\Delta}\left(\bar{u}_j\bar{\phi} + \tau(u_j,\phi)\right) \tag{14}$$

The transposition in space of equation (13) is

$$\beta_{x_i}(\phi) = \frac{\partial\Delta}{\partial x_i}\frac{\partial\bar{\phi}}{\partial\Delta} \tag{15}$$

As a result, equation (12) including β_T will be the main functional operator that will be used as a base throughout the following work to get the filtered Navier-Stokes and PITM equations of turbulent flows.

3 Filtered Navier-Stokes equation

Using equation (4), the exact filtered equation of mass conservation is

$$\frac{\partial\bar{u}_j}{\partial x_j} - \beta_{x_j}(u_j) = 0 \tag{16}$$

and considering the functional operator (12), the filtered Navier-Stokes equation for the motion reads

$$\begin{aligned}\frac{\partial\bar{u}_i}{\partial t} + \frac{\partial\left(\bar{u}_i\bar{u}_j\right)}{\partial x_j} - \beta_T(u_i) = &-\frac{1}{\rho}\frac{\partial\bar{p}}{\partial x_i} + \frac{1}{\rho}\beta_{x_i}(p) - \frac{\partial\tau(u_i,u_j)}{\partial x_j} \\ +\nu\frac{\partial^2\bar{u}_i}{\partial x_j\partial x_j} - \nu\frac{\partial^2\Delta}{\partial x_j\partial x_j}\frac{\partial\bar{u}_i}{\partial\Delta} &- \nu\frac{\partial\Delta}{\partial x_j}\frac{\partial\Delta}{\partial x_j}\frac{\partial^2\bar{u}_i}{\partial\Delta^2} - 2\nu\frac{\partial\Delta}{\partial x_j}\frac{\partial^2\bar{u}_i}{\partial x_j\partial\Delta}\end{aligned} \tag{17}$$

Equation (17) is of very complex mathematical form due to the commutation terms appearing in left and right-hand sides of equation (17). With the aim to get a more tractable equation, we account for the commutation terms only in the material derivative considering that the other terms act only in the near wall region and can be therefore neglected in the core flow. A deeper reason to do that is that the main contribution of the commutation terms to the changes in turbulent energy arises from the convective terms, as will be detailed in equation (26) of section 4. Furthermore, these terms lead to a clear interpretation of the additional flux in the spectral space, as shown in equation (76) of section 7 and which corresponds to an important physical effect, the energy exchange due to the variation of the subfilter cutoff. So that equation (17) reduces to

$$\frac{\partial\bar{u}_i}{\partial t} + \frac{\partial(\bar{u}_i\bar{u}_j)}{\partial x_j} - \beta_T(u_i) = -\frac{1}{\rho}\frac{\partial\bar{p}}{\partial x_i} + \nu\frac{\partial^2\bar{u}_i}{\partial x_j\partial x_j} - \frac{\partial\tau(u_i,u_j)}{\partial x_j} \tag{18}$$

where β_T is given by

$$\beta_T(u_i) = \frac{\partial \Delta}{\partial t}\frac{\partial \bar{u}_i}{\partial \Delta} + \frac{\partial \Delta}{\partial x_j}\frac{\partial}{\partial \Delta}\left(\bar{u}_j\bar{u}_i + \tau(u_j, u_i)\right) \tag{19}$$

Or equivalently,

$$\beta_T(u_i) = \left[\frac{\partial \Delta}{\partial t} + \bar{u}_j\frac{\partial \Delta}{\partial x_j}\right]\frac{\partial \bar{u}_i}{\partial \Delta} + \bar{u}_i\frac{\partial \Delta}{\partial x_j}\frac{\partial \bar{u}_j}{\partial \Delta} + \frac{\partial \Delta}{\partial x_j}\frac{\partial \tau(u_j, u_i)}{\partial \Delta} \tag{20}$$

We suppose that the commutation terms in the material derivative of equation (20) are dominant in comparison with the other ones for simulation of turbulent flows in a practical way. In this case, assuming also that the derivative $\partial\tau(u_i, u_j)/\partial\Delta$ can be neglected in comparison with the other terms, we get the simpler expression

$$\beta_T(u_i) \approx \left[\frac{\partial \Delta}{\partial t} + \bar{u}_j\frac{\partial \Delta}{\partial x_j}\right]\frac{\partial \bar{u}_i}{\partial \Delta} = \frac{D\Delta}{Dt}\frac{\partial \bar{u}_i}{\partial \Delta} \tag{21}$$

Note that this commutation term included in the motion equation (18) has the effect to slightly modify the coupling between the filtered velocity $\bar{u}_i$ and the turbulent stress field. In fact, they are the commutation terms appearing in the transport equation of the subfilter scale stresses that are of primary importance in PITM.

4 Exact subfilter scale stress equation

The main ingredient of the PITM method is the new dissipation-rate equation that constitutes the cornerstone of the modeling. This equation is used in conjunction with the transport equation of the subfilter scale turbulent energy or the subfilter scale stress (SFS) depending on the closure level that is chosen. In a general framework, we need to establish the transport equation for the stress tensor $\tau(u_i, u_j) = \overline{u_i u_j} - \bar{u}_i\bar{u}_j$ which is composed of two terms. To do it, we consider first the transport equation of the tensor formed by the double velocities $t_{ij} = u_i u_j$

$$\frac{dt_{ij}}{dt} = -\frac{1}{\rho}\left(u_j\frac{\partial p}{\partial x_i} + u_i\frac{\partial p}{\partial x_j}\right) + \nu\left(u_j\frac{\partial^2 u_i}{\partial x_k\partial x_k} + u_i\frac{\partial^2 u_j}{\partial x_k\partial x_k}\right) \tag{22}$$

Once again, we apply the functional operator (12) with $\phi = t_{ij}$ for computing the filtered term appearing in the left hand side of this equation

$$\overline{\frac{dt_{ij}}{dt}} = \frac{\partial \bar{t}_{ij}}{\partial t} + \frac{\partial}{\partial x_k}\left(\bar{u}_k\bar{t}_{ij}\right) + \frac{\partial \tau(u_k, t_{ij})}{\partial x_k} - \beta_T(t_{ij}) \tag{23}$$

The transport equation for the quantity $\bar{u}_i\bar{u}_j$ is obtained by multiplying equation (18) by $\bar{u}_j$ and adding the transposed equation. As a result, we finally find that the transport equation for $\tau(u_i, u_j)$ including the commutation terms in the convection process reads

$$\begin{aligned}
&\frac{\partial \tau(u_i, u_j)}{\partial t} + \frac{\partial}{\partial x_k}\big(\tau(u_i, u_j)\bar{u}_k\big) - \beta_T(u_i u_j) + \bar{u}_j\beta_T(u_i) + \bar{u}_i\beta_T(u_j) \\
&= -\frac{\partial \tau(u_i, u_j, u_k)}{\partial x_k} + \nu\frac{\partial^2 \tau(u_i, u_j)}{\partial x_k\partial x_k} - \frac{1}{\rho}\frac{\partial \tau(p, u_i)}{\partial x_j} - \frac{1}{\rho}\frac{\partial \tau(p, u_j)}{\partial x_i} + \tau\left(p, 2S_{ij}\right) \\
&-2\nu\tau\left(\frac{\partial u_i}{\partial x_k}, \frac{\partial u_j}{\partial x_k}\right) - \tau(u_i, u_k)\frac{\partial \bar{u}_j}{\partial x_k} - \tau(u_j, u_k)\frac{\partial \bar{u}_i}{\partial x_k}
\end{aligned} \tag{24}$$

with the general definitions $\tau(f,g) = \overline{fg} - \bar{f}\bar{g}$ and $\tau(f,g,h) = \overline{fgh} - \bar{f}\tau(g,h) - \bar{g}\tau(h,f) - \bar{h}\tau(f,g) - \bar{f}\bar{g}\bar{h}$ for any turbulent quantities f, g, h and where S_{ij} denotes the tensor of the strain deformation

$$S_{ij} = \frac{1}{2}\left(\frac{\partial u_i}{\partial x_j} + \frac{\partial u_j}{\partial x_i}\right) \tag{25}$$

The commutation terms appearing in equation (24) takes a very complex form but in practice, we retain only the commutation terms of higher magnitude in equation (24) linked to the derivatives $\partial\tau(u_i,u_j)/\partial\Delta$ leading to the approximate equation

$$\beta_T(u_iu_j) - \bar{u}_j\beta_T(u_i) - \bar{u}_i\beta_T(u_j) \approx \frac{D\Delta}{Dt}\frac{\partial\tau(u_i,u_j)}{\partial\Delta} \tag{26}$$

5 Modeled PITM equations

The subfilter scale stress transport equation is obtained from the modeling of the exact equation (24). For the sake of clarity, we denote the subfilter scale stress as $(\tau_{ij})_{sfs} = \tau(u_i,u_j)$ and the subfilter scale energy as $k_{sfs} = \tau(u_i,u_i)/2$. This transport equation for $(\tau_{ij})_{sfs}$ can be written in the compact form as

$$\frac{\partial(\tau_{ij})_{sfs}}{\partial t} + \frac{\partial}{\partial x_k}\big((\tau_{ij})_{sfs}\bar{u}_k\big) = P_{ij} + \Pi_{ij} - \frac{2}{3}\delta_{ij}\epsilon_{sfs} + J_{ij} \tag{27}$$

where P_{ij}, Π_{ij} and J_{ij} denote the production, redistribution and diffusion terms and ϵ_{sfs} is the subfilter-scale dissipation rate. The production term P_{ij} is composed by the production P^1_{ij} due to the interaction between the subfilter-scale stress and the filtered velocity gradient

$$P^1_{ij} = -(\tau_{ik})_{sfs}\frac{\partial\bar{u}_j}{\partial x_k} - (\tau_{jk})_{sfs}\frac{\partial\bar{u}_i}{\partial x_k} \tag{28}$$

and by the commutation term P^2_{ij} caused by the commutation term defined by equation (26) involving the derivative of the filter width

$$P^2_{ij} = \frac{D\Delta}{Dt}\frac{\partial(\tau_{ij})_{sfs}}{\partial\Delta} \tag{29}$$

The redistribution term Π_{ij} is modeled into a slow part Π^1_{ij} which characterizes the return to isotropy due to the action of turbulence on itself and a rapid part Π^2_{ij} which describes the return to isotropy by action of the filtered velocity gradient as

$$\Pi^1_{ij} = -c_1\frac{\epsilon_{sfs}}{k_{sfs}}\left((\tau_{ij})_{sfs} - \frac{2}{3}k_{sfs}\,\delta_{ij}\right) \tag{30}$$

and

$$\Pi^2_{ij} = -c_2\left(P^1_{ij} - \frac{1}{3}P^1_{mm}\delta_{ij}\right) \tag{31}$$

where c_1 is the Rotta coefficient modified to account for the spectrum splitting whereas c_2 remains the same as in statistical modeling. The diffusion term J_{ij} is modeled assuming a well known gradient law hypothesis

$$J_{ij} = \frac{\partial}{\partial x_k}\left(\nu \frac{\partial (\tau_{ij})_{sfs}}{\partial x_k} + c_s \frac{k_{sfs}}{\epsilon_{sfs}} (\tau_{kl})_{sfs} \frac{\partial (\tau_{ij})_{sfs}}{\partial x_l}\right) \tag{32}$$

where c_s is a constant numerical coefficient. The subfilter scale energy transport equation is obtained from equation (27) by contraction of tensor $(\tau_{ij})_{sfs}$

$$\frac{\partial k_{sfs}}{\partial t} + \frac{\partial}{\partial x_k}\left(k_{sfs}\bar{u}_k\right) = P - \epsilon_{sfs} + J \tag{33}$$

where $P = P_{ii}/2 = P^1 + P^2$ with

$$P^1 = -(\tau_{ij})_{sfs} \frac{\partial \bar{u}_j}{\partial x_i} \tag{34}$$

and

$$P^2 = \frac{D\Delta}{Dt} \frac{\partial k_{sfs}}{\partial \Delta} \tag{35}$$

and $J = J_{mm}/2$. In the case where $\Delta = \Delta(t)$, the commutation term appearing in equation (35) reduces to

$$P^2 = \frac{\partial \Delta}{\partial t} \frac{\partial k_{sfs}}{\partial \Delta} \tag{36}$$

whereas in the case where $\Delta = \Delta(x_i)$, it is given by

$$P^2 = \bar{u}_j \frac{\partial \Delta}{\partial x_j} \frac{\partial k_{sfs}}{\partial \Delta} \tag{37}$$

The subfilter dissipation-rate ϵ_{sfs} equation including the commutation terms is modeled as

$$\frac{\partial \epsilon_{sfs}}{\partial t} + \frac{\partial}{\partial x_k}\left(\epsilon_{sfs}\bar{u}_k\right) = c_{\epsilon_1} \frac{\epsilon_{sfs}}{k_{sfs}} P - c_{\epsilon_{2sfs}} \frac{\epsilon_{sfs}^2}{k_{sfs}} + J_\epsilon \tag{38}$$

where J_ϵ denotes the diffusion term modeled as

$$J_\epsilon = \frac{\partial}{\partial x_j}\left(\nu \frac{\partial \epsilon_{sfs}}{\partial x_j} + c_\epsilon \frac{k_{sfs}}{\epsilon_{sfs}} (\tau_{jm})_{sfs} \frac{\partial \epsilon_{sfs}}{\partial x_m}\right) \tag{39}$$

and where c_ϵ is a constant coefficient. As mentioned by Chaouat and Schiestel (2005, 2012), the coefficient $c_{\epsilon_{2sfs}}$ is now a linear function of the ratio of the subfilter energy to the total energy k_{sfs}/k that is calibrated using a general Von Kármán spectrum $E(\kappa)$ defined as

$$E(\kappa) = \frac{\frac{2}{3}\beta(\kappa L_e)^{\alpha-1} L_e k}{\left[1 + \beta(\kappa L_e)^\alpha\right]^{1+\gamma}} \tag{40}$$

where $\alpha\gamma = 2/3$, $\beta = (3C_K/2)^{-\gamma}$ and $C_K \approx 1.45$ is the Kolmogorov constant, $L_e = k^{3/2}/\epsilon$, verifying $\lim_{\kappa\to\infty} E(\kappa) = C_K \epsilon^{2/3}\kappa^{-5/3}$, leading to

$$c_{\epsilon_{2sfs}}(\eta_c) = c_{\epsilon_1} + \frac{c_{\epsilon_2} - c_{\epsilon_1}}{\left[1 + \beta\eta_c^\alpha\right]^\gamma} \tag{41}$$

and where the parameter η_c is defined as

$$\eta_c = \kappa_c L_e = \frac{\pi}{\Delta} \frac{k^{3/2}}{\epsilon} \tag{42}$$

referring to the total energy $k = \langle k_{sfs} \rangle + \langle k_{les} \rangle$ and the total dissipation-rate $\epsilon = \langle \epsilon_{sfs} \rangle + \langle \epsilon_{les} \rangle$. This parameter acts like a dynamic parameter which depends on the location of the cutoff within the energy spectrum. In equation (42), Δ is the effective filter width around the cell Ω which is computed by

$$\Delta = \Delta_a \left(\zeta + (1 - \zeta) \frac{\Delta_b}{\Delta_a} \right) \tag{43}$$

where the filters lengths Δ_a and Δ_b are defined by $\Delta_a = (\Delta_1 \Delta_2 \Delta_3)^{1/3}$ and $\Delta_b = (\Delta_1^2 + \Delta_2^2 + \Delta_3^2)/3)^{1/2}$ and ζ is a parameter set to 0.8. As a result, the function $c_{\epsilon_{2sfs}}$ introduced in equation (38) then controls the relative amount of turbulence energy contained in the subfilter range during the computation. Assuming that the large and small scale fluctuations are uncorrelated, the total stress τ_{ij} then reads (Chaouat and Schiestel, 2007; Chaouat, 2017a)

$$\tau_{ij} = \langle (\tau_{ij})_{sfs} \rangle + \langle (\tau_{ij})_{les} \rangle \tag{44}$$

where the resolved scale energy tensor is defined as

$$(\tau_{ij})_{les} = \bar{u}_i \bar{u}_j - \langle u_i \rangle \langle u_j \rangle \tag{45}$$

The statistical average of the resolved stress which corresponds to the correlation of the large scale fluctuating velocities is computed by a numerical procedure using the relation

$$\langle (\tau_{ij})_{les} \rangle = \langle \bar{u}_i \bar{u}_j \rangle - \langle \bar{u}_i \rangle \langle \bar{u}_j \rangle = \left\langle u_i^< u_j^< \right\rangle \tag{46}$$

where $u_i^< = \bar{u}_i - \langle u_i \rangle$ and $u_i^>$ denote the large and small scale fluctuating velocities, respectively. The average of the subfilter scale stress is

$$\langle (\tau_{ij})_{sfs} \rangle = \langle \overline{u_i u_j} \rangle - \langle \bar{u}_i \bar{u}_j \rangle = \left\langle u_i^> u_j^> \right\rangle \tag{47}$$

Consequently, the Reynolds stress tensor given by equation (44) reads

$$\tau_{ij} = \left\langle u_i^> u_j^> \right\rangle + \left\langle u_i^< u_j^< \right\rangle \tag{48}$$

The statistical turbulent energy is obtained as half the trace of equation (44)

$$k = \langle k_{sfs} \rangle + \langle k_{les} \rangle \tag{49}$$

The resolved part of the dissipation rate ϵ_{les} corresponds to the correlation of the large-scale fluctuating velocities. The low Reynolds number formulation of the subfilter scale model is given in Appendix A with the functions listed in Table 1.

6 Numerical estimate of extra terms arising from the non-commutativity

6.1 Velocities

The commutation term introduced in the mass equation (16) is given by equation (15) and the one appearing in the motion equation (18) is given by equation (21). The calculus of $\beta_T(\phi)$ requires to evaluate the derivative $\partial\overline{\phi}/\partial\Delta$. In the present case, following the method of Iovieno and Tordella (2003), this derivative is computed by applying a second filtering operation with a larger filter width leading to

$$\frac{\partial\bar{\phi}}{\partial\Delta} = \lim_{\delta\Delta\to 0} \frac{\bar{\phi}(\bar{\Delta}+\delta\bar{\Delta}) - \bar{\phi}(\bar{\Delta})}{\delta\bar{\Delta}} \approx \frac{\bar{\phi}(\tilde{\bar{\Delta}}) - \bar{\phi}(\bar{\Delta})}{\tilde{\bar{\Delta}} - \bar{\Delta}} \tag{50}$$

where $\bar{\Delta}$ is the filter width of the grid-size Δ, and $\tilde{\bar{\Delta}}$ denotes the superfilter width of Δ. The approximation (50) can be applied easily for the velocities $\phi = u_i$

$$\frac{\partial\bar{u}_i}{\partial\Delta} \approx \frac{\bar{u}_i(\tilde{\bar{\Delta}}) - \bar{u}_i(\bar{\Delta})}{\tilde{\bar{\Delta}} - \bar{\Delta}} = \frac{\tilde{\bar{u}}_i - \bar{u}_i}{\tilde{\bar{\Delta}} - \bar{\Delta}} \tag{51}$$

but it deserves a special attention for the stresses $\phi = \tau_{ij}$.

6.2 Turbulent stresses

The commutation term appearing in equation (27) and defined by equation (26) involving the derivative of the subfilter scale stress $(\tau_{ij})_{sfs}$ with respect to the filter width $\bar{\Delta}$ is computed by

$$\frac{\partial(\tau_{ij})_{sfs}}{\partial\Delta} \approx \frac{(\tau_{ij})_{sfs}(\tilde{\bar{\Delta}}) - (\tau_{ij})_{sfs}(\bar{\Delta})}{\tilde{\bar{\Delta}} - \bar{\Delta}} = \frac{(\widetilde{\overline{u_i u_j}} - \tilde{\bar{u}}_i\tilde{\bar{u}}_j) - (\overline{u_i u_j} - \bar{u}_i\bar{u}_j)}{\tilde{\bar{\Delta}} - \bar{\Delta}} \tag{52}$$

Equation (52) can be rewritten in a more practical form involving the stresses $(\tau_{ij})_{sfs} = \overline{u_i u_j} - \bar{u}_i\bar{u}_j$ and $\widetilde{(\tau_{ij})_{sfs}} = \widetilde{\overline{u_i u_j}} - \widetilde{\bar{u}_i\bar{u}_j}$ by

$$\frac{\partial(\tau_{ij})_{sfs}}{\partial\Delta} \approx \frac{\widetilde{(\tau_{ij})_{sfs}} - (\tau_{ij})_{sfs} + (\widetilde{\bar{u}_i\bar{u}_j} - \tilde{\bar{u}}_i\tilde{\bar{u}}_j)}{\tilde{\bar{\Delta}} - \bar{\Delta}} \tag{53}$$

As equation (53) is difficult to use in practice, we prefer to derive a more practical formulation. For any variable ϕ, we have shown in section 2 that $\langle\bar{\phi}\rangle \approx \langle\phi\rangle$ if the filter width is not too large. This approximation can be used to simplify equation (53). Indeed, the first term appearing in equation (53) is small because its statistical average approaches zero

$$\left\langle \widetilde{(\tau_{ij})_{sfs}} - (\tau_{ij})_{sfs} \right\rangle = \left\langle \widetilde{\overline{u_i u_j}} - \widetilde{\bar{u}_i\bar{u}_j} \right\rangle - \langle \overline{u_i u_j} - \bar{u}_i\bar{u}_j \rangle \approx 0 \tag{54}$$

On the other hand, the second term $(\widetilde{\bar{u}_i\bar{u}_j} - \tilde{\bar{u}}_i\tilde{\bar{u}}_j)$ appearing in equation (53) can be developed using the relative velocity u_i^* defined as $u_i^* = \bar{u}_i - \tilde{\bar{u}}_i$ as follows

$$\widetilde{\bar{u}_i\bar{u}_j} - \tilde{\bar{u}}_i\tilde{\bar{u}}_j = \widetilde{\tilde{\bar{u}}_i\tilde{\bar{u}}_j} + \widetilde{\tilde{\bar{u}}_i u_j^*} + \widetilde{\tilde{\bar{u}}_j u_i^*} + \widetilde{u_i^* u_j^*} - \tilde{\bar{u}}_i\tilde{\bar{u}}_j \tag{55}$$

In a first approximation, considering the higher terms in the right hand side of this equation, it a simple matter to show that this equation (55) reduces to

$$\widetilde{\bar{u}_i\bar{u}_j} - \tilde{\bar{u}}_i\tilde{\bar{u}}_j \approx \widetilde{u_i^* u_j^*} \tag{56}$$

So that equation (53) can be reasonably well approximated in a statistical sense by

$$\frac{\partial \left\langle (\tau_{ij})_{sfs} \right\rangle}{\partial \Delta} \approx \frac{\left\langle \widetilde{u_i^* u_j^*} \right\rangle}{\tilde{\bar{\Delta}} - \bar{\Delta}} \tag{57}$$

that is the essential contribution of the commutation term for the stresses. The derivative of the subfilter turbulent energy with respect to the filter width is given by contraction of the tensor $(\tau_{ij})_{sfs}$ in equation (57)

$$\frac{\partial \left\langle k_{sfs} \right\rangle}{\partial \Delta} \approx \frac{1}{2}\frac{\left\langle \widetilde{u_i^* u_i^*} \right\rangle}{\tilde{\bar{\Delta}} - \bar{\Delta}} \tag{58}$$

6.3 Discrete approximation to the top hat filter

In practice, the variable $\bar{\phi}(\tilde{\bar{\Delta}})$ is determined by applying a discrete approximation to the top hat filter written in the form as (Vichnevetsky, 1982; Geurts and van der Bos, 2005)

$$\bar{\phi}(\tilde{\bar{\Delta}}, x_i) = G(\bar{\phi})(\bar{\Delta}, x_i) = \sum_{m \in Z} a_m \bar{\phi}(\bar{\Delta}, x_{i+m}) \tag{59}$$

where a_m are numerical coefficients. The effect of Δ on a Fourier mode $\phi = \exp{(i\kappa x)}$ is given by

$$G(\phi)(x_i) = \sum_{m \in N} a_m \cos(m\kappa\Delta)\exp(i\kappa x_i) = \mathcal{G}(\kappa\Delta)\phi(x_i) \tag{60}$$

The coefficients a_m are determined in the spectral space by satisfying the conditions $\mathcal{G}(0) = 1$, $\mathcal{G}(\pi) = 0$ and $\partial^n\mathcal{G}/\partial\kappa^n = 0$ at $\kappa = 0$ for $n \in N$ in order to get a function as flat as possible in the neighborhood of $\kappa = 0$ (Vichnevetsky, 1982). As a result, it is found that the filter of second order accuracy in space is given by $a_0 = 1/2$, $a_1 = a_{-1} = 1/4$ and $a_m = 0$ for $|m| \geq 2$ whereas for the fourth-order filter, $a_0 = 5/8$, $a_1 = a_{-1} = 1/2$, $a_2 = a_{-2} = -1/8$ and $a_m = 0$ for $|m| \geq 4$. For the second order accurate filter, note that the trapezoidal rule applied to the top hat filter coincides with the spectral method yielding the same coefficient values a_m. The formulation of the discrete second order accurate filter (59) can be extended to the case of non-uniform filter width using the trapezoidal rule. In this case, the variable $\tilde{\bar{\phi}}$ is computed as

$$\tilde{\bar{\phi}}_i = \frac{\bar{\phi}_{i-1}(\bar{\Delta}_{i-1} + \bar{\Delta}_i) + \bar{\phi}_i(2\bar{\Delta}_i + \bar{\Delta}_{i-1} + \bar{\Delta}_{i+1}) + \bar{\phi}_{i+1}(\bar{\Delta}_i + \bar{\Delta}_{i+1})}{2\bar{\Delta}_{i-1} + 4\bar{\Delta}_i + 2\bar{\Delta}_{i+1}} \tag{61}$$

The super filter width $\tilde{\bar{\Delta}}_i$ is computed as $\tilde{\bar{\Delta}}_i = \bar{\Delta}_i + (\bar{\Delta}_{i-1} + \bar{\Delta}_{i+2})/2$. Taking into account equation (61), it is then simple matter to show that the derivative $\partial\bar{\phi}/\Delta$ is obtained by

$$\left(\frac{\partial\bar{\phi}}{\partial\Delta}\right)_i = \frac{\bar{\phi}_{i-1}(\bar{\Delta}_{i-1} + \bar{\Delta}_i) - \bar{\phi}_i(2\bar{\Delta}_i + \bar{\Delta}_{i-1} + \bar{\Delta}_{i+1}) + \bar{\phi}_{i+1}(\bar{\Delta}_i + \bar{\Delta}_{i+1})}{(\bar{\Delta}_{i-1} + 2\bar{\Delta}_i + \bar{\Delta}_{i+1})(\bar{\Delta}_{i-1} + \bar{\Delta}_{i+1})} \tag{62}$$

The algorithm (62) can be easily implemented in CFD codes to compute the commutation terms on varying grids. Moreover, equation (62) indicates that the commutation error is of second order effect $O(\bar{\Delta})^2$ with respect to the filter-width.

7 Interpretation of the commutation term in the spectral space

It is possible to calculate the derivative of the statistical subfilter turbulent energy $\langle k_{sfs} \rangle$ with respect to the grid-size Δ considering the density spectrum $E(\kappa)$ as follows

$$\frac{\partial \langle k_{sfs} \rangle}{\partial \Delta} = \frac{\partial \langle k_{sfs} \rangle}{\partial \kappa_c} \frac{\partial \kappa_c}{\partial \Delta} = \frac{\partial \kappa_c}{\partial \Delta} \frac{\partial}{\partial \kappa_c} \int_{\kappa_c}^{\infty} E(\kappa) d\kappa = \frac{\kappa_c^2 E(\kappa_c)}{\pi} \tag{63}$$

The density spectrum $E(\kappa)$ is given by equation (40), so that the derivative $\partial \langle k_{sfs} \rangle / \partial \Delta$ can be calculated as follows

$$\frac{\partial \langle k_{sfs} \rangle}{\partial \Delta} = \frac{2}{3} \beta (\pi L_e)^{\alpha} \left(\frac{\langle k_{sfs} \rangle}{k} \right)^{\frac{\gamma+1}{\gamma}} \frac{k}{\Delta^{\alpha+1}} \tag{64}$$

In the case where the cutoff wave number is placed in the inertiel zone of the spectrum, equation (64) leads to

$$\frac{\partial \langle k_{sfs} \rangle}{\partial \Delta} = \frac{2}{3} \frac{\langle k_{sfs} \rangle}{\Delta} \tag{65}$$

Equation (64) can be an alternative to the use of equation (58) that requires to perform numerical calculations. But even if equation (64) is simple to apply, we prefer however to consider equation (58) because it guaranties that the gain or loss of energy in the resolved part of the spectrum is exactly recovered in the modeled part of the spectrum at each grid-point of the mesh during the simulation. The connection with the spectral space is obtained by introducing the additional flux of energy transfer $\mathcal{K}(\kappa_c)$ which results from the variation of the spectrum splitting. In the case of simulation of homogeneous turbulence performed on a varying grid-size in time $\Delta = \Delta(t)$, the transport equation in a statistical sense of the subfilter turbulent energy reads (Schiestel, 1987; Chaouat and Schiestel, 2007; Chaouat and Schiestel, 2013)

$$\frac{\partial \langle k_{sfs} \rangle}{\partial t} = P(\kappa_c, \kappa_d) + \mathcal{F}(\kappa_c) + \mathcal{K}(\kappa_c) - \epsilon \tag{66}$$

where

$$P(\kappa_c, \kappa_d) = -\int_{\kappa_c}^{\kappa_d} \varphi_{ij}(\kappa) \frac{\partial \langle u_i \rangle}{\partial x_j} d\kappa = -\langle (\tau_{ij})_{sfs} \rangle \frac{\partial \langle u_i \rangle}{\partial x_j} \tag{67}$$

and

$$\mathcal{F}(\kappa_c) = -\int_0^{\kappa_c} \mathcal{T}(\kappa) d\kappa = \int_{\kappa_c}^{\infty} \mathcal{T}(\kappa) d\kappa \tag{68}$$

where κ_d is the dissipative wave number, $\varphi_{ij}(\kappa)$ is the spherical mean of the Fourier transform of the two-point fluctuating velocity correlation tensor (Cambon, 1981; Schiestel, 1987; Chaouat and

Schiestel, 2007), $\mathcal{T}(\kappa)$ denotes the spectral transfer term and $\mathcal{K}(\kappa_c)$ is the additional flux of energy transfer resulting from the variation in the cutoff location given by

$$\mathcal{K}(\kappa_c) = -E(\kappa_c)\frac{\partial \kappa_c}{\partial t} \tag{69}$$

In equation (66), the dissipation-rate ϵ is interpreted as a spectral flux defined by $\epsilon = \mathcal{F}(\kappa_d)+\mathcal{K}(\kappa_d)$. Equation (66) allows to determine the role played by the term involving the variation of the cutoff wave number on the modeled/resolved scales. In the case where the grid-size increases in time $\partial\Delta(t)/\partial t > 0$ or $\mathcal{K}(\kappa_c) > 0$, then a part of the energy contained into the resolved scales is removed and fed into the modeled spectral zone, whereas on the contrary, when $\partial\Delta(t)/\partial t < 0$ or $\mathcal{K}(\kappa_c) < 0$, a part of energy coming from the modeled zone is injected into the resolved scales. The flux transfer $\mathcal{K}(\kappa_c)$ can be developed into the form as

$$\mathcal{K}(\kappa_c) = -E(\kappa_c)\frac{\partial \kappa_c}{\partial t} = -E(\kappa_c)\frac{\partial \kappa_c}{\partial \Delta}\frac{\partial \Delta}{\partial t} = \frac{\partial \langle k_{sfs}\rangle}{\partial \Delta}\frac{\partial \Delta}{\partial t} \tag{70}$$

showing clearly that it is a function of the derivative of the subfilter energy to the grid-size. One can see that the flux transfer $\mathcal{K}(\kappa_c)$ given by equation (70) exactly corresponds to the commutation term (36) involved in the transport equation for the subfilter energy (33). It is possible to obtain a theoretical expression for $\mathcal{K}(\kappa_c)$ by substituting (64) into equation (70)

$$\mathcal{K}(\kappa_c) = \frac{2}{3}\beta(\pi L_e)^{\alpha}\left(\frac{\langle k_{sfs}\rangle}{k}\right)^{\frac{\gamma+1}{\gamma}}\frac{k}{\Delta^{\alpha+1}}\frac{\partial \Delta}{\partial t} \tag{71}$$

In parallel with equation (66), the transport equation of the subfilter scale stress $\langle(\tau_{ij})_{sfs}\rangle$ reads (Schiestel, 1987; Chaouat and Schiestel, 2007; Chaouat and Schiestel, 2013)

$$\frac{\partial \langle(\tau_{ij})_{sfs}\rangle}{\partial t} = P_{ij}(\kappa_c,\kappa_d) + \Pi_{ij}(\kappa_c,\kappa_d) + \mathcal{F}_{ij}(\kappa_c) + \mathcal{K}_{ij}(\kappa_c) - \epsilon_{ij} \tag{72}$$

where the different terms appearing in this equation are, respectively, the production, redistribution, transfer, additional flux due to the variation in the spectrum splitting and dissipation. These terms are defined by

$$P_{ij}(\kappa_c,\kappa_d) = -\int_{\kappa_c}^{\kappa_d}\left[\varphi_{ik}(\kappa)\frac{\partial \langle u_i\rangle}{\partial x_k} + \varphi_{jk}(\kappa)\frac{\partial \langle u_j\rangle}{\partial x_k}\right]d\kappa \tag{73}$$

$$\Pi_{ij}(\kappa_c) = \int_{\kappa_c}^{\kappa_d}\psi_{ij}(\kappa)d\kappa \tag{74}$$

$$\mathcal{F}_{ij}(\kappa_c) = -\int_0^{\kappa_c}\mathcal{T}_{ij}(\kappa)d\kappa = \int_{\kappa_c}^{\infty}\mathcal{T}_{ij}(\kappa)d\kappa \tag{75}$$

and

$$\mathcal{K}_{ij}(\kappa_c) = -\varphi_{ij}(\kappa_c)\frac{\partial \kappa_c}{\partial t} \tag{76}$$

The additional flux $\mathcal{K}_{ij}(\kappa_c)$ corresponds to the production term P^2_{ij} given by equation (29) in case where $\Delta = \Delta(t)$.

8 Realizability conditions

The issue to address when performing numerical simulations of turbulent flows in CFD is to get physical solutions that are as close as possible to real flows. Many tools allow to improve the numerical solution given by the solving of the Navier-Stokes equations and turbulence model. Among these tools, one deals with the realizability conditions. The constraint of realizability requires that the Reynolds stress tensor τ_{ij} satisfies the conditions (Schumann, 1977; Speziale et al., 1994)

$$\tau_{ii} \geq 0 \tag{77}$$

$$\tau_{ij}^2 - \tau_{ii}\tau_{jj} \leq 0 \tag{78}$$

$$det(\tau_{ij}) \geq 0 \tag{79}$$

where the summation convention is suspended in equations (77) and (78). Obviously, these relations concerned with the Reynolds stress tensor τ_{ij} also hold for the subfilter scale stress tensor $(\tau_{ij})_{sfs}$ in LES simulation when only the small scales are modeled. This question was examined by Vreman et al. (1994) for the exact subfilter scale stress and its modeling through several eddy viscosity models. First at all, these authors used the mathematical definition (1) of the filtering operation to calculate the exact subfilter scale stress from its definition $(\tau_{ij})_{sfs} = \tau(u_i, u_j)$. As a result, the tensor $(\tau_{ij})_{sfs}$ was formulated into the mathematical form as

$$(\tau_{ij})_{sfs}(\boldsymbol{x}) = \int_\Omega G\left[\boldsymbol{x} - \boldsymbol{\xi}, \Delta(\boldsymbol{x}, t)\right]](u_i(\boldsymbol{\xi}) - \bar{u}_i(\boldsymbol{x})(u_j(\boldsymbol{\xi}) - \bar{u}_j(\boldsymbol{x})]\, d\boldsymbol{\xi} \tag{80}$$

showing that the stress tensor forms a Gram matrix of inner products composed by the velocity $v_i(\boldsymbol{x}, \boldsymbol{\xi}) = u_i(\boldsymbol{\xi}) - \bar{u}_i(\boldsymbol{x})$ that is positive semi definite if the filter kernel G is positive. As a consequence, the exact tensor $(\tau_{ij})_{sfs}$ then satisfies the realizability conditions if the top hat filter or Gaussian filter is used in the filtering process. But the spectral cutoff filter that can produce negative values of G does not satisfy the realizability conditions. Taking into account this argument, we will discard the spectral cutoff filter and we will consider the top hat filter (60) in this work because it is the more convenient in practice. We now analyze the modeled subfilter tensor $(\tau_{ij})_{sfs}$ given by its transport equation (27). Because of its complex form, it is not possible to examine whether $(\tau_{ij})_{sfs}$ verifies inequalities (77), (78) and (79) [36]. The only way to guarantee realizability in the hierarchy of second moment closure is via the weak form of realizability which requires that when a principal subfilter scale stress component vanishes, its time derivative must be positive to prevent negative values of the normal subfilter stress components to appear (Speziale et al., 1994). In a first step, we consider the case of homogeneous turbulence that is the starting point to analyze the question of realizability and examine this question in a coordinate system aligned with the principal axes of the stress tensor (Chaouat and Schiestel, 2009). In the principal axes of coordinate, equation (27) can be written in the compact form as

$$\frac{\partial(\tau_{ii}^*)_{sfs}}{\partial t} = P_{ii}^{1*} + \frac{\partial \Delta}{\partial t}\frac{\partial(\tau_{ii}^*)_{sfs}}{\partial \Delta} + \Pi_{ii}^* - \frac{2}{3}\epsilon_{sfs} \tag{81}$$

where in a general way the tensor ϕ_{ij}^* denotes the tensor ϕ_{ij} expressed in the principal axes of coordinate and where the Einstein convention is now suspended for repeated indices ii. When the stress component $(\tau^*_{ii})_{sfs}$ vanishes, it can be seen that the production term expressed in the principal axes P^*_{ii} goes to zero so that the weak form of the realisability condition finally implies the constraint

$$c_1 \geqslant 1 - \frac{1}{\epsilon_{sfs}} \left(c_2 P^1 + \frac{3}{2} \frac{\partial \Delta}{\partial t} \frac{\partial (\tau^*_{ii})_{sfs}}{\partial \Delta} \right) \tag{82}$$

to be verified. From the formulation of the subfilter scale stress model indicated in Appendix A, we know that the function c_1 is greater than unity and that the function c_2 is positive. So that inequality (82) is verified if

$$c_2 P^1 + \frac{3}{2} \frac{\partial \Delta}{\partial t} \frac{\partial (\tau^*_{ii})_{sfs}}{\partial \Delta} \geqslant 0 \tag{83}$$

As the production term of the turbulent energy P is usually positive, and greater than the magnitude of the commutation errors, the constraint (82) is usually verified implying that the model satisfies the weak form of realizability. If this reasoning is correct in most cases, note however that the production term incidentally can be negative in second moment closure. This situation corresponds to the case of backscatter effect when energy is transferred from small scales to large scales. We need then to analyze the sign of the commutation term to know what is its effect on inequality (83). As shown by equation (64) as well as (58), the derivative of the statistical subfilter turbulent energy with respect to the grid-size Δ is positive. We assume that this relation holds for the instantaneous subfilter energy, so that $\partial (\tau^*_{ii})_{sfs}/\partial \Delta > 0$. As a consequence, the sign of the commutation term is given by the sign of the derivative $\partial \Delta/\partial t$. As a result, when the grid-size increases in time, the commutation term is positive and enforces the realizability condition whereas when Δ decreases, the reverse situation occurs, the commutation term is negative and weakens the realizability conditions. If the present analysis has been conducted for homogeneous flows, one can mention however that realizability violation can be computationally occurred when performing inhomogeneous flows. But from a physical point of view, the diffusion term (32) in equation (81) has a stabilizing effect on the motion equation and tends on the contrary to strengthen the realizability conditions (Chaouat, 2011).

9 Numerical schemes

The numerical simulations are performed using the numerical code developed by Chaouat (2011) based on a finite volume technique including a Runge-Kutta scheme of fourth-order accuracy in time with a combination of a quasi-centered scheme of fourth-order accuracy in space. To improve the stability of the numerical scheme, equations (33), (27) and (38) are integrated in time by an implicit iterative algorithm (Chaouat, 2011). Previous simulations have shown that this numerical code was able to reproduce fairly well a large variety of turbulent flows such as for instance the decaying turbulence (Chaouat and Schiestel, 2009, 2013), flows with wall mass injection (Chaouat and Schiestel, 2005), rotating flows (Chaouat, 2012), flows with separation and reattachment of the boundary layer (Chaouat 2010; Chaouat and Schiestel, 2013), wind tunnel flows (Chaouat, 2017b).

10 Fully developed turbulent channel flow

The fully developed turbulent channel flow is a well documented test case to determine the effect of a varying grid-size on turbulence including statistical data of mean velocity and Reynolds stresses (Ghosal and Moin, 1995; Fröhlich et al., 2007). For that purpose, we simulate the turbulent flow in a computational domain as shown on Fig. 1. The simulations are performed on meshes accounting for a varying grid-size in the streamwise direction x_1 determined by a sudden grid step increase that is akin to grid discontinuities in the flow direction as well as a progressive grid refinement in the normal direction to the wall x_3 to accurately capture the velocity boundary layer. The dimensions of the channel in the streamwise, spanwise and normal directions along the axes x_1, x_2, x_3 are $L_1 = m\delta$, $L_2 = 1.5\delta$ and $L_3 = \delta$, respectively, where m is an integer coefficient depending on the case considered, $m = 9$ for a mesh of a uniform grid-size and $m = 16$ for a mesh of increasing grid-size in the streamwise direction. In order to get a solution that does not depend on the inlet flow at $x_1 = 0$, the channel is here decomposed into two distinct domains. In the first domain between $x_1 = 0$ and 3δ, we generate the fully developed turbulent channel flow on a uniform mesh in the streamwise direction by solving the flow equations and applying a periodic condition between the inlet and outlet. In the second domain between $x_1 = 3\delta$ and $m\delta$, we apply an inflow condition at $x_1 = 3\delta$ that corresponds to the flow solution of the first domain passing through the section at $x_1 = 3\delta$ and a pressure condition at the exit section of the channel. To get a periodic flow in the first domain, a constant pressure gradient term $G_\tau = 2\rho_\tau u_\tau^2/\delta$ is then incorporated in the motion equation to balance the friction at the upper and lower walls. For the whole channel, a periodic boundary condition is applied in the spanwise direction x_2 so that the flow is homogeneous in this direction. No slip velocity condition is imposed at the upper and lower walls. This numerical procedure is very practical because we perform only one computation instead of two computations that must be afterward matched at the interface. It is then possible to study the effect of the varying mesh on the numerical solution without any contamination or potential source of errors of the inlet flow. The grid-size ratio of the mesh in the second domain is defined by $\Delta_1 = f(x_1)\Delta_0$ where Δ_0 is the uniform grid-size and f, a given hyperbolic function. The mesh is uniform in the spanwise direction. In the normal direction to the wall, the grid points are distributed in different spacings with a refinement near the wall according to the transformation

$$x_{3j} = \frac{1}{2}\tanh\left[\xi_j\, F(\xi_j)\,\mathrm{atanh}\, a\right] \tag{84}$$

where $\xi_j = -1 + 2(j-1)/(N_3-1)$ $(j = 1, 2, \cdots N_3)$, F is a function introduced to moderate the refinement near the wall, $F(\xi_j) = \sqrt{(1+\xi_j^2)/2}$, the parameter a is a coefficient set to 0.990 for $N_3 = 84$. Numerical simulations of the spatially developing channel flow are performed at the Reynolds number $R_\tau = u_\tau\delta/2\nu = 395$ based on the averaged friction velocity u_τ and the channel half width $\delta/2$, leading to the bulk Reynolds Reynolds number $R_m = u_m\delta/\nu \approx 13750$, where u_m denotes the bulk velocity. Several PITM simulations are carried out to assess the effect of the filter width on the solution. First at all, PITM1 is performed on the uniform mesh for comparison purpose. Then, PITM2 and PITM3 are performed on the non-uniform mesh accounting for the increasing grid-size in the streamwise direction with and without the commutation terms included in equations. In the present case, we will consider the commutation terms arising only from

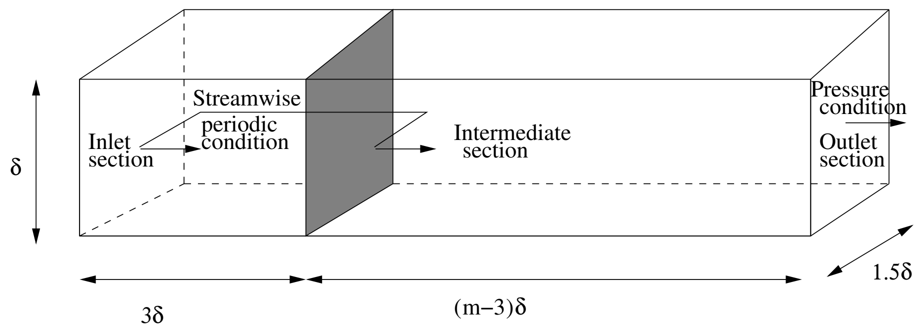

Figure 1: Setup of the numerical channel flow simulations

the sudden grid step increase of the grid-size in the streamwise direction and not the commutation terms caused by the slow varying grid-size in the direction normal to the walls. In the first domain, the dimensionless distances $\Delta^+ = \Delta u_\tau/\nu = (2R_\tau L_i)/(N_i\delta)$ in wall unit are $\Delta_1^+ = 50$, $\Delta_2^+ = 25$, respectively and $\Delta_3^+ \leq 18.3$ whereas in the second domain, Δ_1^+ increases up to 400. Note that the dimensionless coordinate x_3/δ is simply linked to the wall unit coordinate x_3^+ by the relation $x_3/\delta = x_3^+/2R_\tau$ where $x_3^+ = x_3 u_\tau/\nu$. The simulation is compared with data of direct numerical simulation (Moser et al., 1999).

10.1 Uniform grid-size in the streamwise direction

This case with uniform grid-size is worked out to illustrate the feasibility of the numerical procedure and to serve as a benchmark for the case with varying grid-size. The PITM1 simulation of the spatially developing channel flow is performed on a mesh of $144\times48\times84$ grid points. Fig. 2 shows the streamwise variation of the dimensionless pressure versus the x_1 axis coordinate. One can see that the pressure is almost uniform in the first part of the channel because of the periodic condition which is applied between the inlet section at $x_1 = 0$ and the intermediate section at $x_1 = 3\delta$. Then, the pressure gradually decreases when moving to the exit section due to the viscous dissipation effects at the walls. Fig. 3 describes the mean velocity profile $\langle u_1\rangle/u_\tau$ in logarithmic coordinate computed in the first computational domain. The statistics are performed in time and space in the streamwise and spanwise homogeneous directions x_1 and x_2. Overall, one can see that the velocity profile compares very well with the DNS data suggesting that the turbulence model is also well calibrated for predicting confined flows. Moreover, as the grids are sufficiently refined near the walls, the velocity boundary layer is perfectly well reproduced according to the data. Fig. 4 shows the turbulence intensities $\langle(\tau_{ij})_{sfs}\rangle^{1/2}/u_\tau$ and $\langle(\tau_{ij})_{les}\rangle^{1/2}/u_\tau$ associated with the subfilter scales (SFS) and large scales (LES) of the flow. As it can be observed, the core flow in the center of the channel is mainly governed by the large scales whereas the wall flow region is dominated by the subfilter scales because of the presence of the peaks of turbulence in the immediate vicinity of the wall. Fig. 5 displays the profiles of the streamwise, spanwise and normal turbulence intensities normalized by the bulk velocity $\tau_{ii}^{1/2}/u_\tau$. Overall, the shape of the profiles is well recovered. The flow anisotropy is fairly well reproduced in the near wall region even if the level of the streamwise

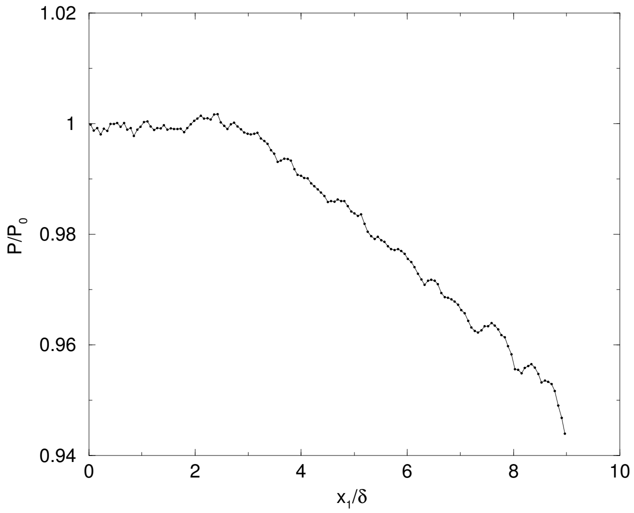

Figure 2: Streamwise variation of the instantaneous pressure P/P_0 versus x_1-axis coordinate. PITM1, •. $R_\tau = 395$.

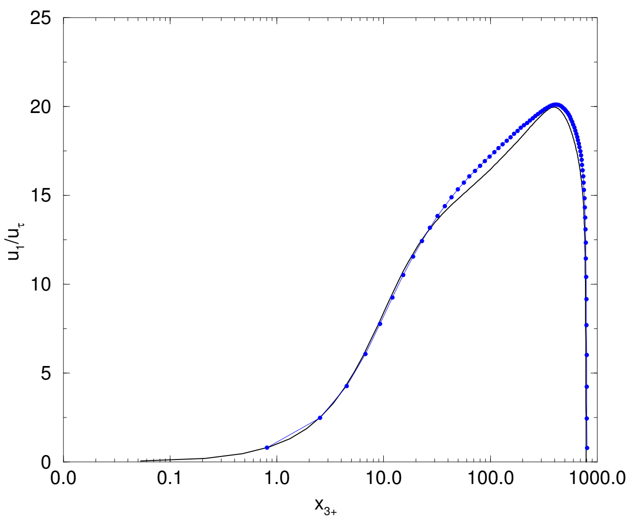

Figure 3: Mean velocity profile $\langle u_1 \rangle / u_\tau$. in logarithmic coordinate. PITM1, •. DNS, — . $R_\tau = 395$.

intensity is however slightly overpredicted while the level of the normal and spanwise intensities are slightly underpredicted in the wall region, probably due to the use of coarse grids in the streamwise and spanwise directions. Fig. 6 shows the profiles of the subfilter energy $\langle k_{sfs} \rangle / u_\tau^2$, resolved energy $\langle k_{les} \rangle / u_\tau^2$, and total energy k/u_τ^2 with the DNS data versus the dimensionless wall coordinate $x_3^+ = x_3 u_\tau / \nu$. As for the turbulent stresses, the shape of the turbulent energy profile

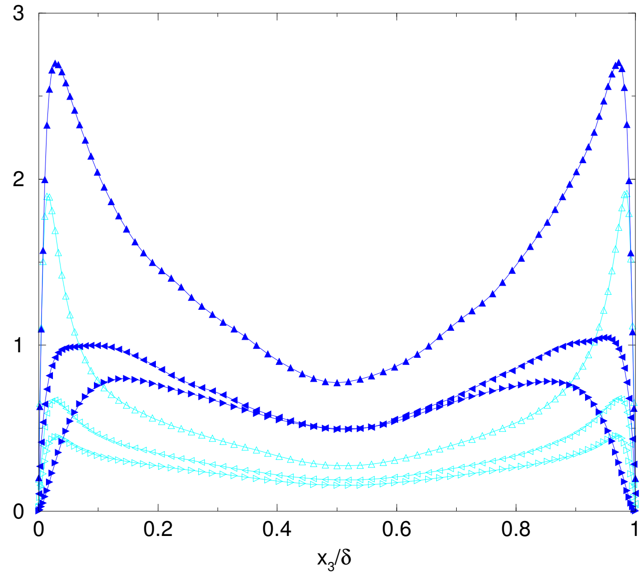

Figure 4: Subfilter and resolved turbulence intensities in wall unit. Subfilter turbulence $\langle(\tau_{ij})_{sfs}\rangle^{1/2}/u_\tau$: ▲, i=1; ◀, i=2; ▶, i=3. Resolved turbulence $\langle(\tau_{ij})_{les}\rangle^{1/2}/u_\tau$: △, i=1; ◁, i=2; ▷, i=3. PITM1: $R_\tau = 395$.

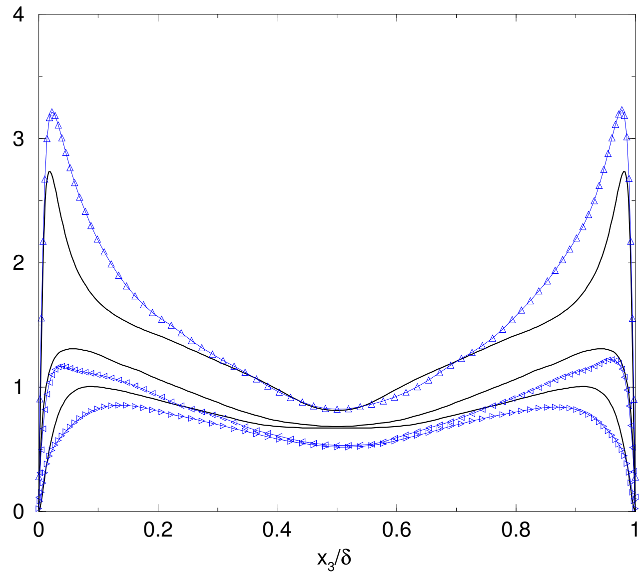

Figure 5: Turbulence intensities in wall unit. $\tau_{ii}^{1/2}/u_\tau$: PITM1: ▲, i=1; ◀, i=2; ▶, i=3. DNS : — . $R_\tau = 395$.

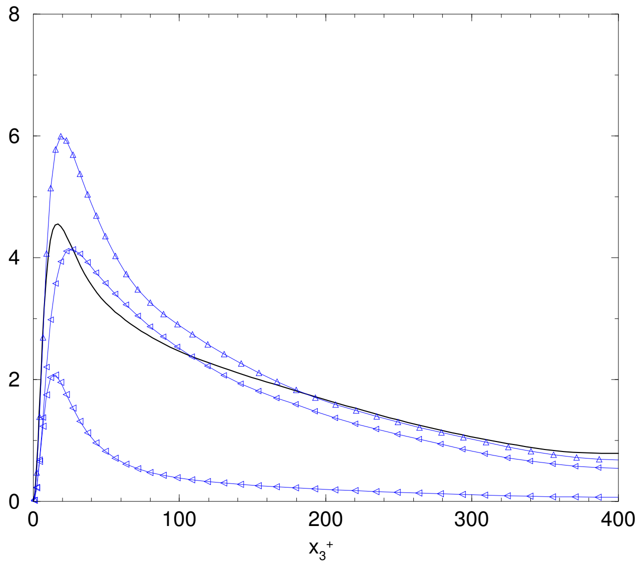

Figure 6: Subfilter energy $\langle k_{sfs}\rangle / u_\tau^2$, resolved energy $\langle k_{les}\rangle / u_\tau^2$, and total turbulent energy k/u_τ^2, versus the wall unit x_3^+. PITM1: $\triangleright$, k_{sfs}; $\triangleleft$, k_{les}; $\triangle$: k. DNS : — . $R_\tau = 395$.

is well recovered but the level of intensity is overpredicted in the near wall region. The agreement with the reference data is however better when moving away from the walls to the core flow. Fig. 7 shows the evolution of the subfilter energy $\langle k_{sfs}\rangle / u_\tau^2$, resolved energy $\langle k_{les}\rangle / u_\tau^2$, and turbulent energy k/u_τ^2, versus the streamwise direction x_1 in the mid-plane of the channel $x_2 = 0.75\delta$, and up to the lower wall at the dimensionless wall distance $x_3^+ = 20$. As a result, all turbulence energies remain almost constant in the entire channel indicating that the slight drop of the pressure occurred in the first domain shown in Fig. 2 has no effect on the turbulence level. Fig. 8 describes the solution trajectories along a vertical line starting from the lower wall towards the upper wall of the channel at the location $x_1 = 3\delta$ that are projected onto the second and third invariant plane in the diagram of Lumley (Lumley, 1978) for the subfilter, resolved and total stresses, respectively. For each diagram, the solution trajectories remain inside the curvilinear triangle that means that the realizability conditions are satisfied. This result was expected for the subfilter scale stresses since it has been demonstrated in section 8 that the turbulence model satisfies the weak form of the realizability conditions with and without the presence of the commutation terms. In that sense, Fig. 8 allows to verify this point at a particular location of the channel. This one was also expected for the resolved scale stresses because of the mathematical form of equation (46). That said, the fact that the total stresses also verify the realizability conditions was not guaranteed by equations but it simply means that the turbulent stresses can be fairly well reconstructed as a whole from the subfilter and resolved stresses. These diagrams also indicate that the PITM simulation is able to reproduce the flow anisotropy that evolves from a two component limit turbulence state near the walls towards a more or less isotropic turbulence state in the center of the channel. On overall, this section demonstrates that the numerical procedure associated with Fig. 1 works well. PITM1

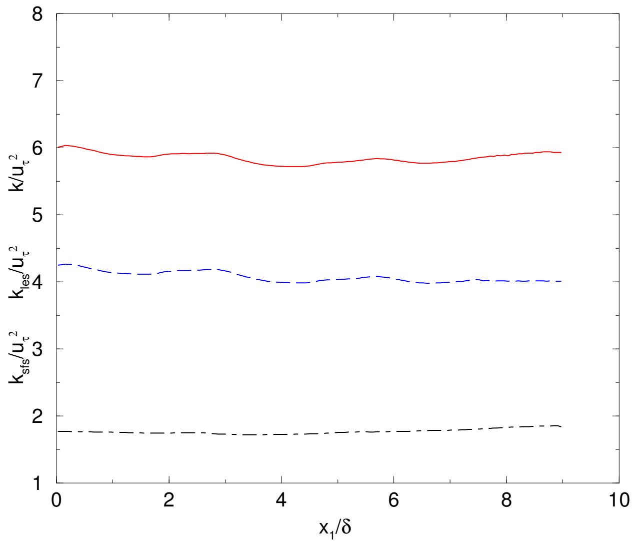

Figure 7: Evolution of the subfilter energy k_{sfs}/u_τ^2, resolved energy k_{les}/u_τ^2, and total turbulent energy k/u_τ^2, in the streamwise direction x_1 at the dimensionless wall distance $x_3^+ = 20$. PITM1: $\bullet$. $R_\tau = 395$.

performed on a such coarse grid provides results that serve as a benchmark in the following section.

10.2 Increasing grid-size in the streamwise direction

The numerical simulations are performed on a mesh of $124 \times 48 \times 84$ grid points. In the first computational domain of the channel, the grid-size Δ_0 is constant while in the second domain, $\Delta(x_1)$ increases according to the function

$$f(x_1) = \frac{5}{2} + \frac{3}{2} \tanh \left[4 \left(\frac{x_1}{\delta} - 5 \right) \right] \tag{85}$$

which approximates locally a step function on few cells of the mesh. This function is chosen such that the ratio of the grid-size $\Delta(x_1)/\Delta_0$ takes on the maximum value 4 as shown by Fig. 9. As it can be observed, this ratio presents a strong variation between $x_1/\delta = 4$ and 7. In practice, such a sudden grid step increase in the grid-size of the mesh occurs when simulating industrial flows in complex geometries. To approach the details of the geometry, the generation of the mesh often leads to locally distorted cells Ω with high variations of the grid-size from one cell to another one. This problem is more acute for unstructured grids. In the present case, as the grid-size in the spanwise and normal directions Δ_2 and Δ_3 is kept constant when moving in the x_1 direction, the effective grid size Δ defined by equation (43) is in fact twice as high as the uniform grid-size. Fig. 10 shows the cross section of the mesh illustrating the grid-size variation in the streamwise direction. The computations are running for a sufficient length time to get statistics that are independent of the initial conditions. For each test case, the statistics are furthermore achieved in time and space in the spanwise homogeneous direction x_2. So that, for any flow variable ϕ, the statistical variable

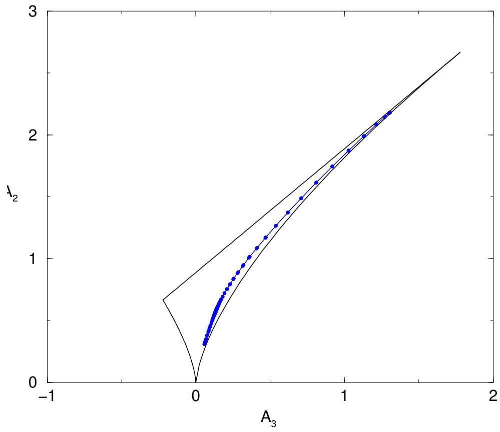

(a)

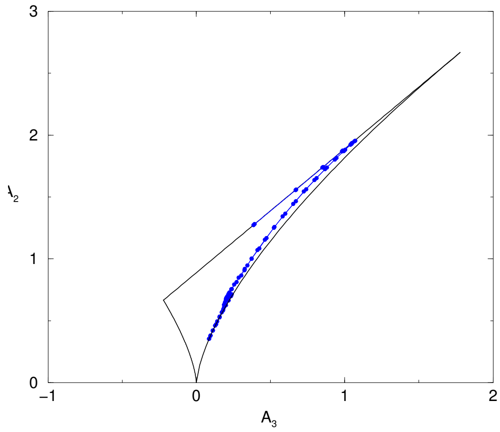

(b)

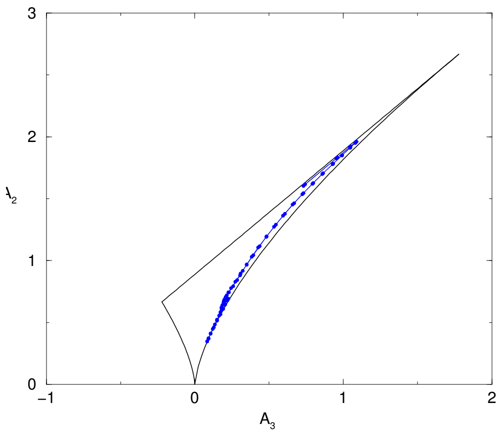

(c)

Figure 8: Solution trajectories along a vertical line in the cross section located at $x_1/\delta = 3$ projected onto the second-invariant/third-invariant plane formed by the anisotropy tensor. (a) Subfilter scale stresses, (b) Resolved scale stresses, (c) Reynolds stresses. PITM1: $\bullet$. $R_\tau = 395$.

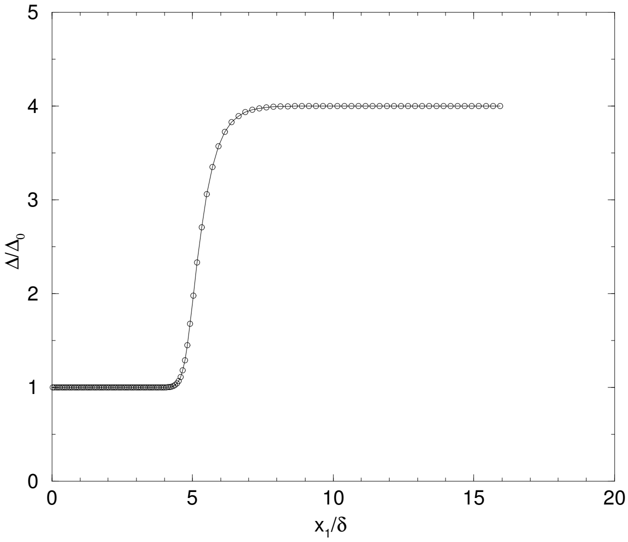

Figure 9: Evolution of the grid-size ratio $\Delta(x_1)/\Delta_0$ in the streamwise direction. $1 \leq \Delta(x_1)/\Delta_0 \leq 4$.

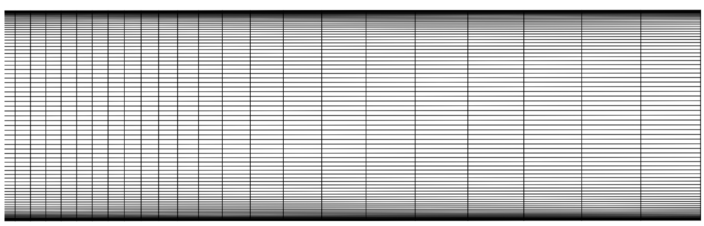

Figure 10: Cross-section of the mesh of $124 \times 48 \times 84$ grid points.

$\langle\phi\rangle$ is a function of x_1 and x_3 coordinates when the convergence is reached. Fig. 11 depicts the evolution of the dimensionless commutation term $\beta_{T*}(u_i) = \beta_T(u_i)\delta/u_m^2$ defined by equation (21) for i=1,2,3 in the mid-plane of the channel at $x_3/\delta = 1/2$ versus the dimensionless distance x_1/δ at a given time. As expected, $\beta_T(u_i)$ is non-zero only in the zone including the sharp variation of the grid-size. To get an insight about the distribution of the commutation errors due to the turbulence, Fig. 12 shows the contours of the the dimensionless commutation term $P_*^2 = P^2\delta/u_\tau^3$ defined by equation (37) in the mid cross section (x_1, x_3) at the spanwise distance $x_2 = 0.75\delta$. This term is computed by means of equation (58) that is a good approximation ensuring positive values. In a first approximation, P^2 reduces to

$$P^2 \approx \bar{u}_1 \frac{\partial\Delta}{\partial x_1}\frac{\partial k_{sfs}}{\partial\Delta} \tag{86}$$

showing its dependence versus the variation of the grid-size $\partial\Delta/\partial x_1$ and the derivative of the subfilter energy with respect to the grid-size $\partial k_{sfs}/\partial\Delta$. As expected, the production term is of higher intensity in the near wall flow region. This term P^2 goes to zero when moving to the center of the channel. Fig. 13 describes the evolution of P^2 in the streamwise direction at $x_3^+ = 20$ $(x_3/\delta = 0.023)$ and $x_3^+ = 50$ $(x_3/\delta = 0.06)$. In the region of the channel where the grid-size Δ varies in space as shown on Fig. 9, the curve exhibits a regular evolution characterized by a sharp increase and decrease of energy production. The commutation term takes on its maximum value at $x_1/\delta = 5$ since the derivative $\partial\Delta/\partial x_1 = 6\Delta_0/\delta$ is highest. Also in accordance with the findings and observations made on Fig. 12, the commutation term is of higher value at $x_3^+ = 50$ than at $x_3^+ = 20$. Fig. 14 shows the evolution of the ratio P^2/P^1 in the streamwise direction both at $x_3^+ = 20$ and at $x_3^+ = 50$, where P^1 is the production of the turbulent energy defined by equation (34). A similar regular evolution as the one observed on Fig. 13 is obtained. The maximum magnitude of the ratio P^2/P^1 is about 15 % at $x_3^+ = 50$ that is appreciable, so one can expect a possible effect of the commutation errors on the solution. In the following, we examine the velocity and stress profiles returned by PITM2 and PITM3 at two sections of the channel at $x_1/\delta = 5$ where $\Delta_1/\Delta_0 = 2.5$ and at $x_1/\delta = 10$ where $\Delta_1/\Delta_0 = 4$. Fig. 15 exhibits the mean velocity profile $\langle u_1\rangle/u_\tau$ in logarithmic coordinate computed at these two locations. Overall, one can see that these profiles compare relatively well with DNS in the boundary layer but the velocities are slightly overpredicted in the center of the channel. In comparison with Fig. 3, the agreement with the DNS data is less favorable. One can remark that this discrepancy is lower at $x_1/\delta = 5$ than at $x_1/\delta = 10$. At a first sight, no significant differences are observed between the PITM2 and PITM3 velocity profiles although the PITM2 velocities are a little bit closer to DNS. This outcome suggests that the accounting for the commutation terms in equations has no major impact on the mean flow velocity, probably due to the fact that PITM is a continuous hybrid RANS-LES non-zonal method. This outcome differs somewhat from the one associated with zonal RANS-LES methods where it is commonly known that the neglect of the commutation terms is responsible for the log-layer mismatch of the velocity profile (Hamba, 2009). Fig. 16 shows the turbulent energy profiles k/u_τ^2 versus the dimensionless wall coordinate $x_3^+ = x_3 u_\tau/\nu$ at $x_1/\delta = 5$ and at $x_1/\delta = 10$. Both simulations return almost the same profile. In particular, the peak of turbulence is overpredicted in the near wall region at $x_3^+ \approx 20$. But at $x_1/\delta = 5$, the turbulence intensity is well predicted in the center of the channel whereas it is under predicted at $x_1/\delta = 10$. As the agreement with the DNS is better at $x_1/\delta = 5$ than at $x_1/\delta = 10$, one can deduce that the solution slightly deteriorates when coarsening the grids. From these Figs., one can see that the effect of the commutation terms on the turbulence is barely noticeable even if PITM2 returns however a turbulence intensity slightly higher for $x_3^+ > 100$ than PITM3 because of the additional production term P^2. To deepen the analysis, it is therefore worth investigating the evolution of the turbulent energy and normal stresses in the streamwise direction x_1 at the wall unit $x_3^+ = 20$ and $x_3^+ = 50$ for both simulations. The value $x_3^+ = 20$ is chosen because the turbulence is very high at this wall distance (see Fig. 6). The one $x_3^+ = 50$ is also considered because the production term P^2 is of higher intensity at $x_3^+ = 50$ than at $x_3^+ = 20$ (see Fig. 13). Fig. 17 shows the evolution of the subfilter and resolved scale turbulent energies as well as the total energy, $\langle k_{sfs} \rangle / u_\tau^2$, $\langle k_{les} \rangle / u_\tau^2$ and k/u_τ^2 normalized by the averaged friction velocity in the streamwise direction x_1 at the wall unit $x_3^+ = 20$. As expected, it is found that the subfilter scale energy increases as the grid-size increases since larger scales must be modeled and vice versa, the resolved scale energy decreases since less scales are computed. Physically, this means that the turbulence model allows to support the smaller eddies of the fine grid-size that are convected into the coarse grid. At first sight, the results are identical for both simulations. But according to the sudden grid step increase of the grid-size (see Fig. 9), the curves associated with PITM2 are however slightly steeper than those associated with PITM3. For both simulations, the total turbulent energy remains relatively constant suggesting that the small part of energy that has been gained by the subfilter scales when passing from the fine grid to the coarse grid is lost by the resolved scales. In comparison with the evolution of the total energy shown in Fig. 7, a slight overshoot of energy occurs at about $x_1/\delta = 5$ for both simulations.

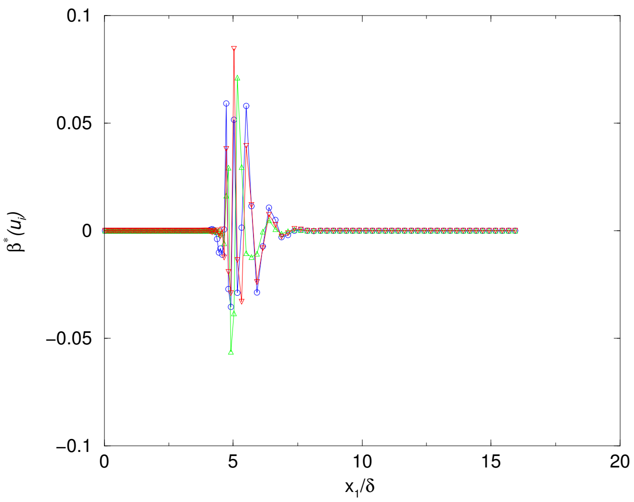

Figure 11: Evolution of the commutation term $\beta_{T*}(u_i) = \beta_T(u_i)\delta/u_m^2$ for i=1,2,3 associated with the velocity given by equation (21) versus the dimensionless distance x_1/δ at $x_3/\delta = 1/2$. $\circ$, i=1; $\triangleleft$, i=2; $\triangledown$, i=3.

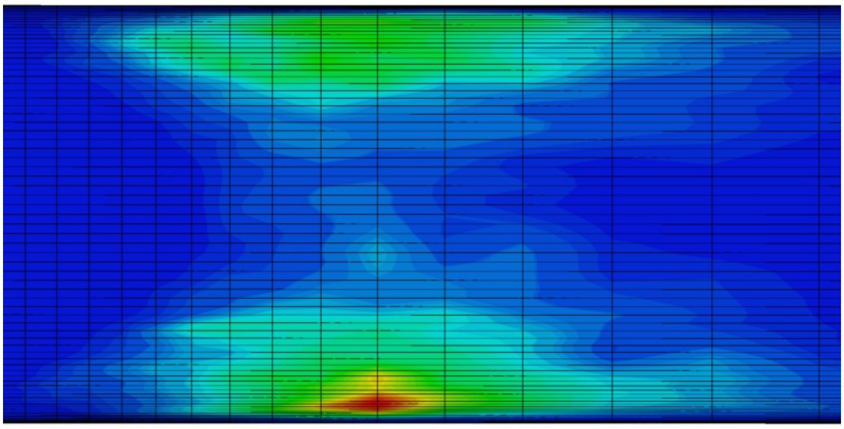

Figure 12: Contours of the commutation term of the instantaneous flow $P_*^2 = P^2\delta/u_\tau^3$ given by equation (37). $0 < P_*^2 < 5$ (from blue to red) in the mid-plane of the channel at $x_2 = 0.75\delta$.

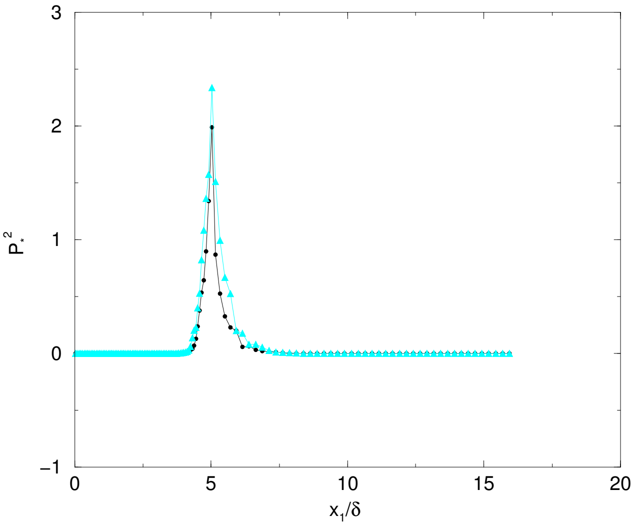

Figure 13: Evolution of the commutation term $P^2_* = P^2\delta/u_\tau^3$ given by equation (37) associated with the turbulent energy versus the dimensionless distance x_1/δ at different wall distance. •, $x_3^+ = 20$; ▲, $x_3^+ = 50$.

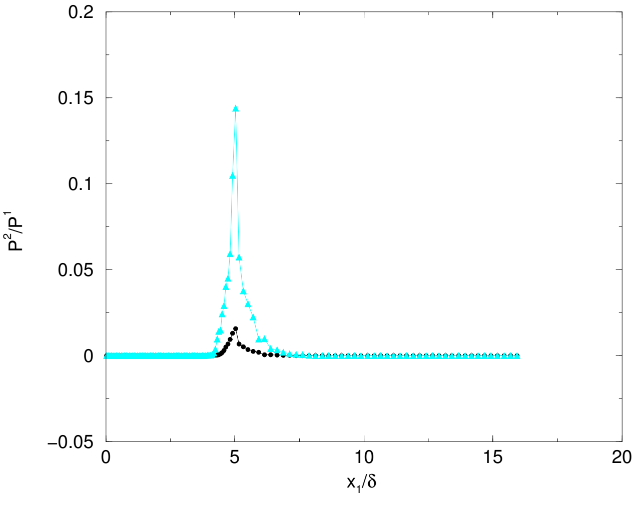

Figure 14: Evolution of the ratio P^2/P^1 versus the dimensionless distance x_1/δ at different wall distance. •, $x_3^+ = 20$; ▲, $x_3^+ = 50$.

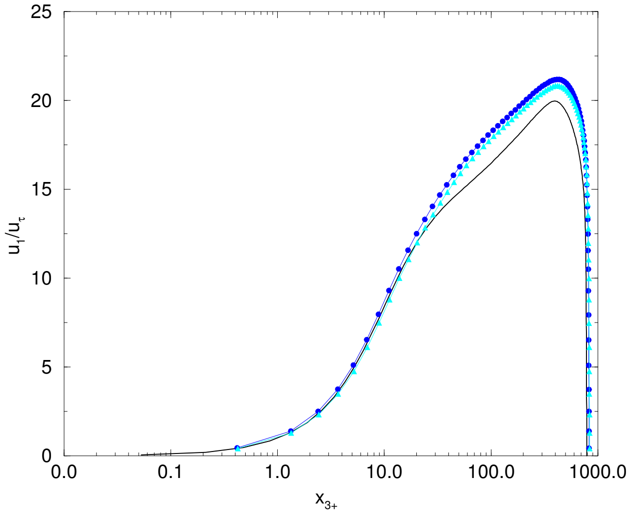

(a)

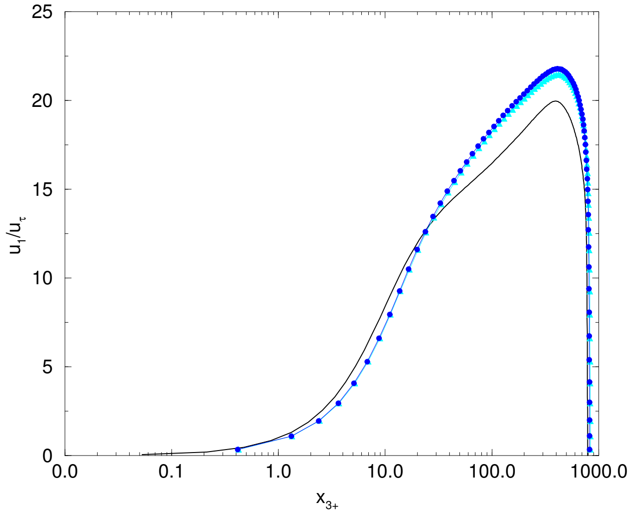

(b)

Figure 15: Mean velocity profile $\langle u_1 \rangle / u_\tau$ in logarithmic coordinate at various locations. (a) $x_1/\delta = 5$, (b) $x_1/\delta = 10$. PITM2, ▲; PITM3, •. DNS, — . $R_\tau = 395$.

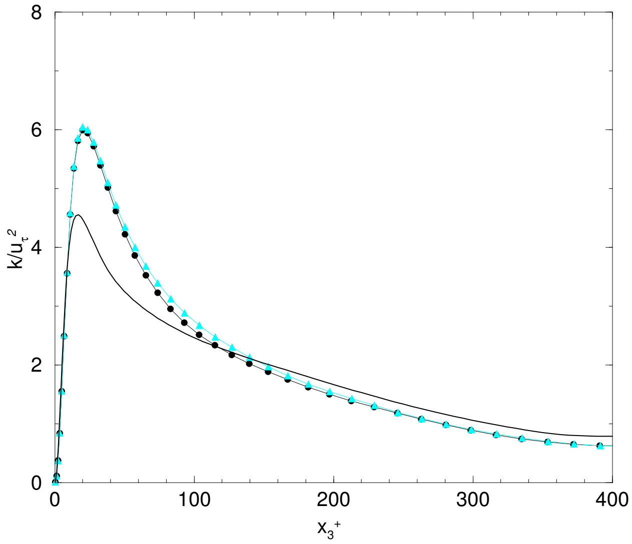

(a)

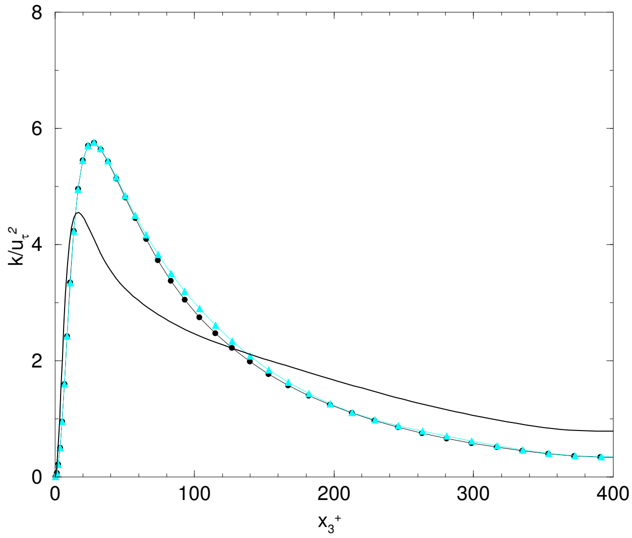

(b)

Figure 16: Turbulent energy k/u_τ^2 at various locations. (a) $x_1/\delta = 5$, (b) $x_1/\delta = 10$. PITM2, ▲; PITM3, •; DNS, — . $R_\tau = 395$.

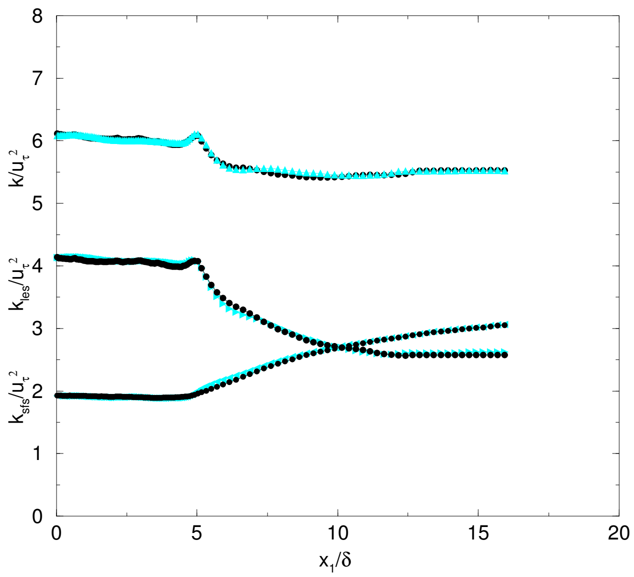

Figure 17: Evolution of the subfilter, resolved and total turbulent energy $\langle k_{sfs}\rangle/u_\tau^2$, $\langle k_{les}\rangle/u_\tau^2$, k/u_τ^2 in the streamwise direction at the dimensionless wall distance $x_3^+ = 20$. PITM2: sfs, ◀; les, ▶; total, ▲. PITM3, •. $R_\tau = 395$.

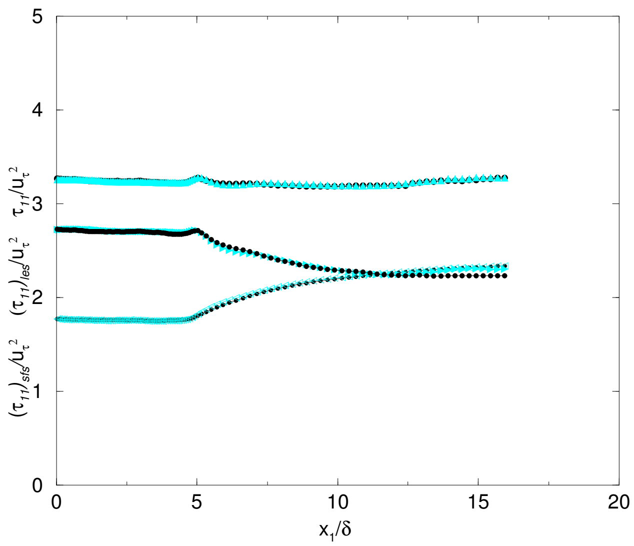

Figure 18: Evolution of the subfilter, resolved and total turbulent stress $\langle(\tau_{11})_{sfs}\rangle/u_\tau^2$, $\langle(\tau_{11})_{les}\rangle/u_\tau^2$, τ_{11}/u_τ^2, in the streamwise direction at the dimensionless wall distance $x_3^+ = 20$. PITM2: sfs, ◀; les, ▶; total, ▲. PITM3, •. $R_\tau = 395$.

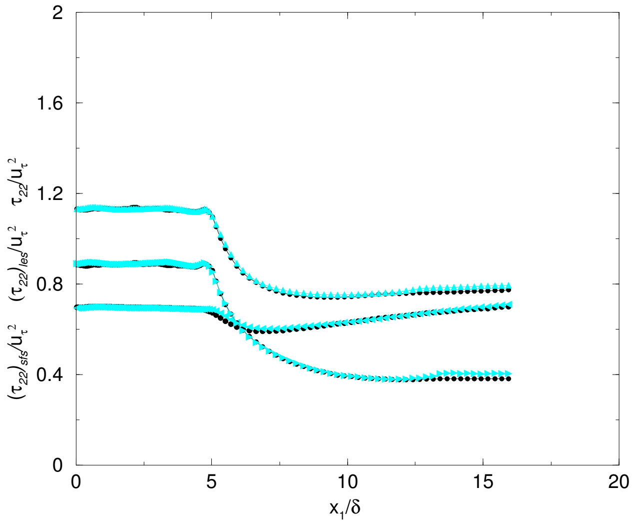

Figure 19: Evolution of the subfilter, resolved and total turbulent stress $\langle(\tau_{22})_{sfs}\rangle/u_\tau^2$, $\langle(\tau_{22})_{les}\rangle/u_\tau^2$, τ_{22}/u_τ^2 in the streamwise direction at the dimensionless wall distance $x_3^+ = 20$. PITM2: sfs, ◀; les, ▶; total, ▲. PITM3, •. $R_\tau = 395$.

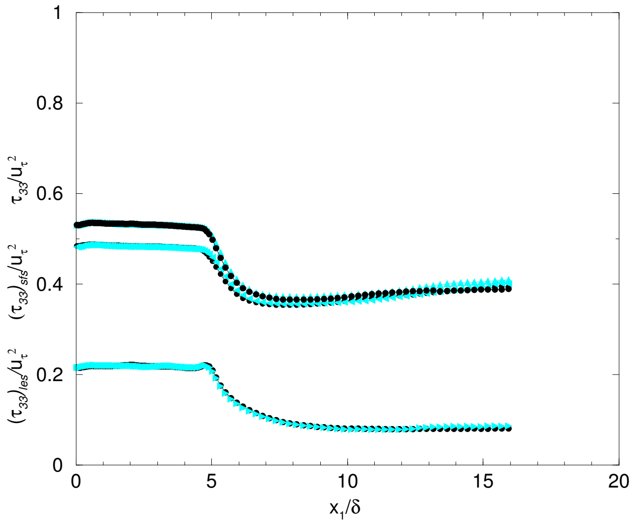

Figure 20: Evolution of the subfilter, resolved and total turbulent stress $\langle(\tau_{33})_{sfs}\rangle/u_\tau^2$, $\langle(\tau_{33})_{les}\rangle/u_\tau^2$, τ_{33}/u_τ^2 in the streamwise direction at the dimensionless wall distance $x_3^+ = 20$. PITM2: sfs, ◀; les, ▶; total, ▲. PITM3, •. $R_\tau = 395$.

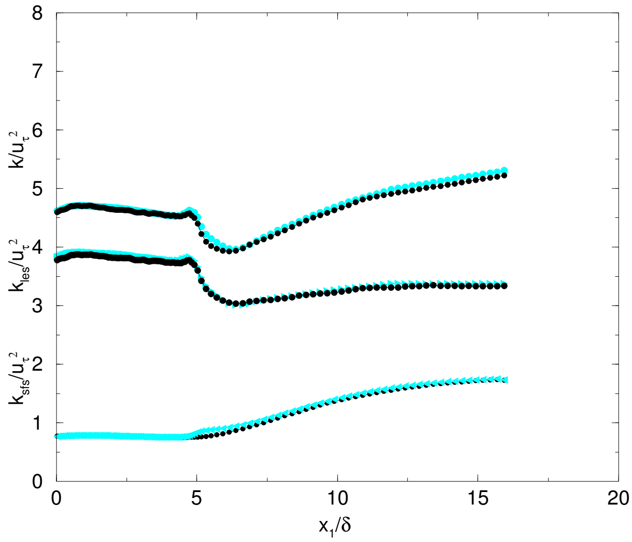

Figure 21: Evolution of the subfilter, resolved and total turbulent energy $\langle k_{sfs}\rangle/u_\tau^2$, $\langle k_{les}\rangle/u_\tau^2$, k/u_τ^2 in the streamwise direction at the dimensionless wall distance $x_3^+ = 50$. PITM2: sfs, ◀; les, ▶; total, ▲. PITM3, •. $R_\tau = 395$.

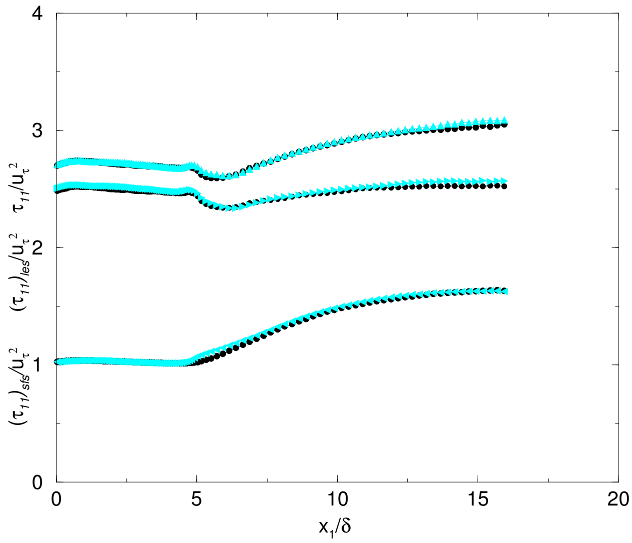

Figure 22: Evolution of the subfilter, resolved and total turbulent stress $\langle(\tau_{11})_{sfs}\rangle/u_\tau^2$, $\langle(\tau_{11})_{les}\rangle/u_\tau^2$, τ_{11}/u_τ^2 in the streamwise direction at the dimensionless wall distance $x_3^+ = 50$. PITM2: sfs, ◀; les, ▶; total, ▲. PITM3, •. $R_\tau = 395$.

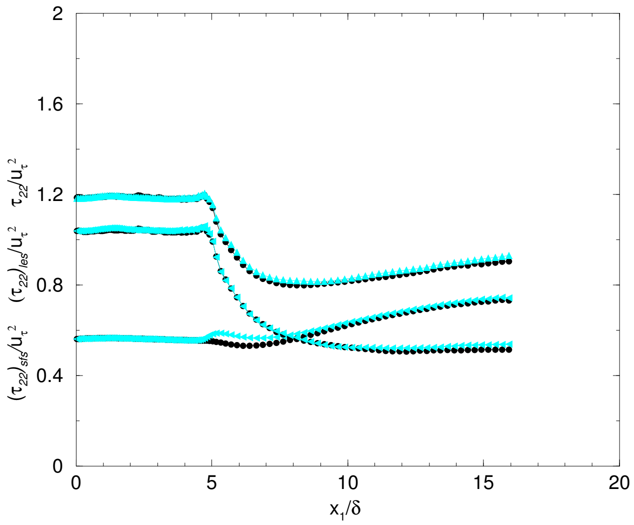

Figure 23: Evolution of the subfilter, resolved and total turbulent stress $\langle(\tau_{22})_{sfs}\rangle/u_\tau^2$, $\langle(\tau_{22})_{les}\rangle/u_\tau^2$, τ_{22}/u_τ^2, in the streamwise direction at the dimensionless wall distance $x_3^+ = 50$. PITM2: sfs, ◀; les, ▶; total, ▲. PITM3, •. $R_\tau = 395$.

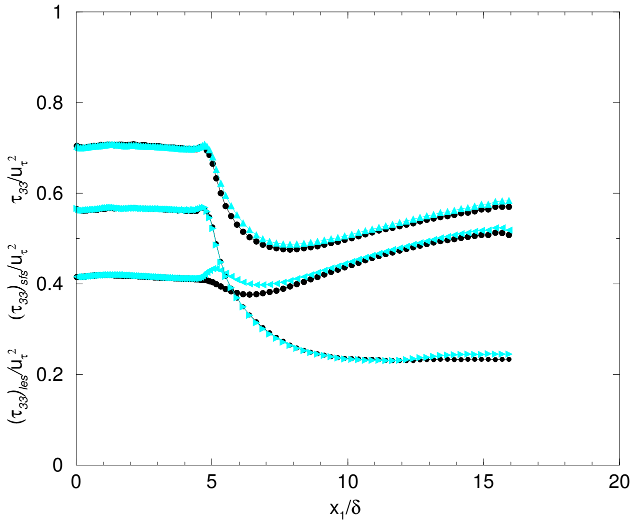

Figure 24: Evolution of the subfilter, resolved and total turbulent stress $\langle(\tau_{33})_{sfs}\rangle/u_\tau^2$, $\langle(\tau_{33})_{les}\rangle/u_\tau^2$, τ_{33}/u_τ^2, in the streamwise direction at the dimensionless wall distance $x_3^+ = 50$. PITM2: sfs, ◀; les, ▶; total, ▲. PITM3, •. $R_\tau = 395$.

The evolution in the streamwise direction of the subfilter, resolved and total stresses normalized by the friction velocity, $\langle(\tau_{ii})_{sfs}\rangle/u_\tau^2$, $\langle(\tau_{ii})_{les}\rangle/u_\tau^2$ and τ_{ii}/u_τ^2, are plotted in Figs. 18, 19, 20. As

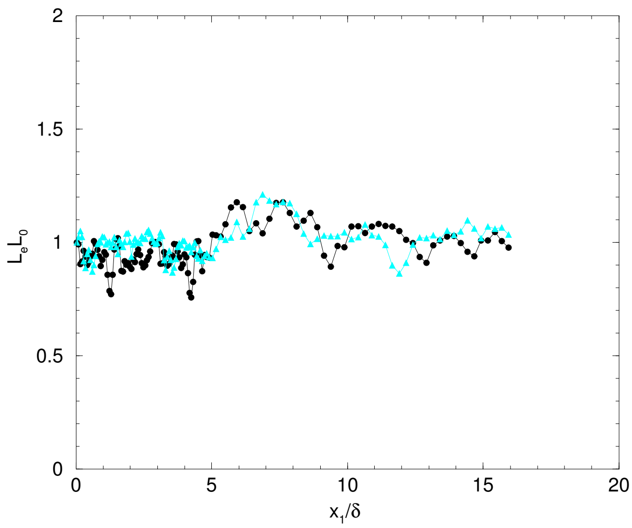

Figure 25: Evolution of the turbulence length-scale $L_e = k^{3/2}/\epsilon$ in the streamwise direction at the dimensionless wall distance $x_3^+ = 20$. PITM2, ▲; PITM3, •. $R_\tau = 395$.

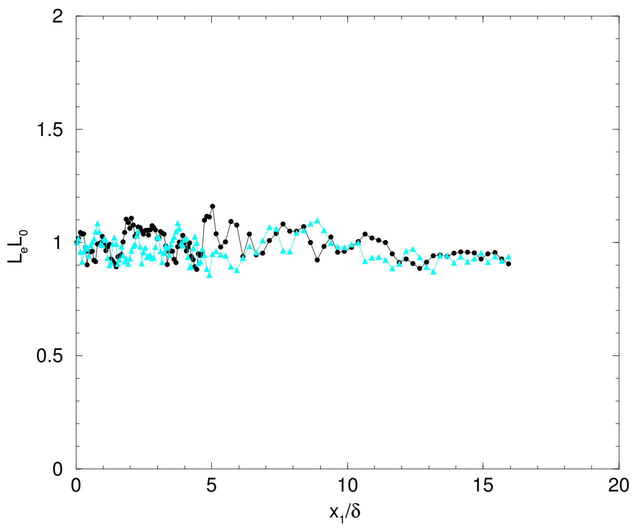

Figure 26: Evolution of the turbulence length-scale $L_e = k^{3/2}/\epsilon$ in the streamwise direction at the dimensionless wall distance $x_3^+ = 50$. PITM2, ▲; PITM3, •. $R_\tau = 395$.

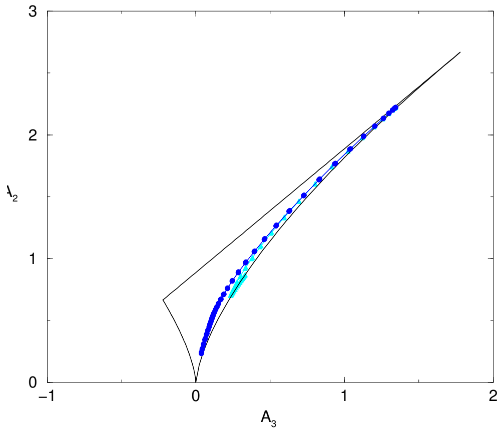

(a)

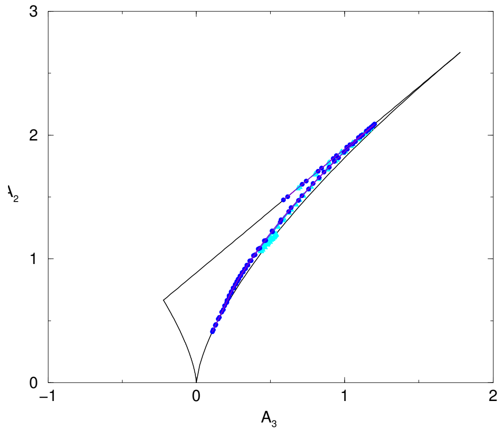

(b)

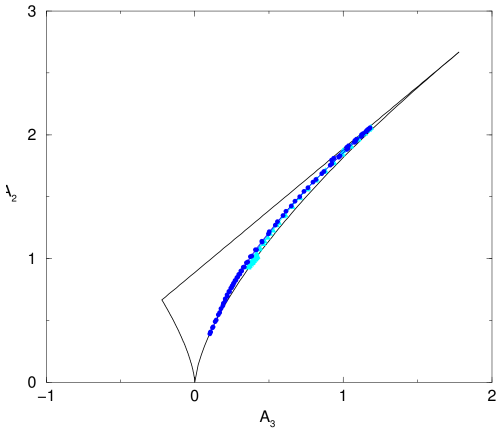

(c)

Figure 27: Solution trajectories along a vertical line in the cross section located at $x_1/\delta = 5$ projected onto the second-invariant/third-invariant plane formed by the anisotropy tensor. (a) Subfilter scale stresses, (b) Resolved scale stresses, (c) Reynolds stresses. PITM2, ▲; PITM3, •. $R_\tau = 395$.

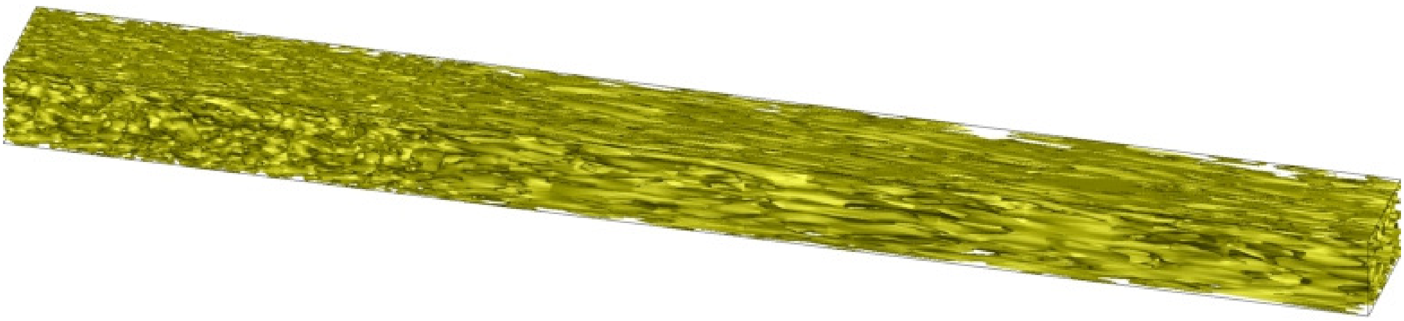

(a)

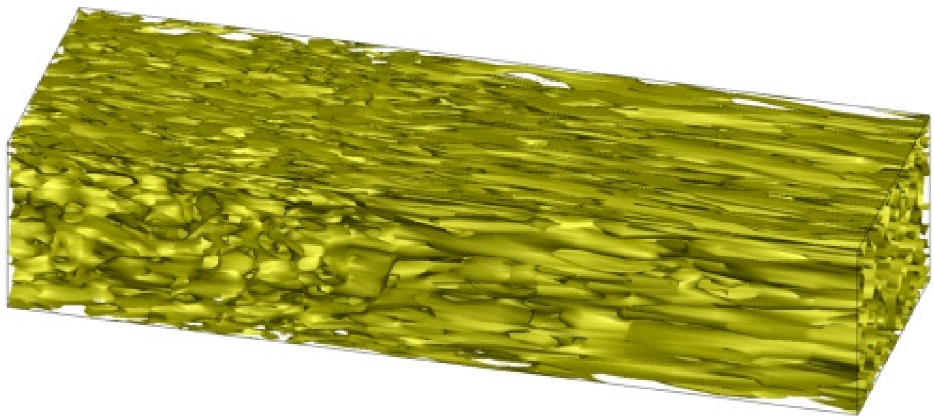

(b)

Figure 28: Vortical activity illustrated by the Q isosurfaces at $R_\tau = 395$, $R_m = 13750$. (Q = 10 s^{-2}). PITM2 simulation $144 \times 48 \times 84$. (a), View in real ratio $[0, 16\delta]$ x $[0, 1.5\delta]$ x $[0, \delta]$. (b), Enlargement view $[3\delta, 8\delta]$ x $[0, 1.5\delta]$ x $[0, \delta]$.

expected for both simulations, Fig. 18 shows that the streamwise subfilter scale stress $\langle(\tau_{11})_{sfs}\rangle$ increases while the streamwise resolved stress $\langle(\tau_{11})_{les}\rangle$ decreases according to the increase of the grid-size, but the total stress τ_{11} remains almost constant, the subfilter scales and resolved scales are just compensating from each other. Figs. 19 and 20 display the evolution of the normal stresses τ_{22} and τ_{33} in the streamwise direction. First at all, it can be noticed that their turbulence intensities are very low in comparison with the one associated with τ_{11}, more precisely, $\tau_{11}/\tau_{22} \approx 3$ while $\tau_{11}/\tau_{33} \approx 6$. The subfilter stress $(\tau_{22})_{sfs}$ is almost constant when passing from the fine grid to the coarse grid but the resolved stress $(\tau_{22})_{les}$ decreases significantly leading to a diminution of the total stress τ_{22}. Surprisingly, the subfilter stress $(\tau_{33})_{sfs}$ (note that $(\tau_{33})_{sfs} > (\tau_{33})_{les}$) slightly decreases when moving from the fine grid to the coarse grid but as expected, the resolved stress $(\tau_{33})_{les}$ also decreases. On overall, it is found that the turbulent stress profiles returned by PITM2 and PITM3 are quite similar from each other suggesting that the accounting for the commutation terms in equations has a weak effect on the results, at least at the wall unit $x_3^+ = 20$. But as shown on Fig. 14, the ratio P^2/P^1 being higher at $x_3^+ = 50$ than at $x_3^+ = 20$, it is worth analyzing these stresses at $x_3^+ = 50$. Figs. 21, 22, 23 and 24 show the evolution of these stresses in the streamwise direction at $x_3^+ = 50$. In particular, Fig. 21 displays the evolution of the subfilter, resolved and total turbulent energies. Although the sharing out of turbulence among the subgrid and resolved scales varies when going from the fine grid to the coarse grid, the total energy reached at $x_1/\delta = 5$ is well recovered at the exit $x_1/\delta = 15$ but a drop of energy has occurred at the beginning of the grid enlargement. It is found that the accounting for the commutation terms has a slight beneficial effect because the diminution of energy is slightly lower for PITM2 than for PITM3. Moreover, in comparison with PITM3, PITM2 tends to reduce the delay in the response of the turbulence model to the variable grid-size ratio, even if the effect of the commutation terms linked to the additional flux transfer $\mathcal{K}(\kappa_c)$ included in equations (33) and (38) of the turbulence model is not too pronounced. When examining the normal stresses plotted in Figs. 22, 23 and 24, one can observe that PITM2 and PITM3 return similar evolution except however for the PITM2 subfilter scale stresses that present a small reincrease of energy just in the region of the grid enlargement due to the accounting for the commutation term P^2. In particular, the normal stresses τ_{22} and τ_{33} are not maintained constant as they should be, but they decrease too much. This shortcoming should be attributed to the grid resolution which is too coarse for the turbulence model to accurately simulate this flow and not to the modeling of the commutation terms accounting for the material derivate of the filter width $D\Delta/Dt$. Figs. 25 and 26 describe the evolution of the turbulence length-scale $Le = k^{3/2}/\epsilon$ in the streamwise direction in the horizontal plane located both at $x_3^+ = 20$ and $x_3^+ = 50$. For both PITM simulations, the turbulence length-scale remains almost constant when moving from the fine grid to the coarse grid. This result is not surprising here since it has been verified from Figs. 17 and 21 that the total energy $k = \langle k_{sfs}\rangle + \langle k_{les}\rangle$ is kept perfectly constant at $x_3^+ = 20$ and roughly constant at $x_3^+ = 50$. We know obviously that the dissipation-rate ϵ is not affected by the cutoff wave number $\kappa_c = \pi/\Delta$. Fig. 27 shows the solution trajectories along a vertical line in the cross section located at $x_1/\delta = 5$ projected onto the second and third invariant associated with PITM2 and PITM3. One can see that the realizability conditions are still satisfied for the subfilter, resolved and total stresses. There is no discernible difference between PITM2 and PITM3 results indicating that both flows are similar to each other. With the aim to get qualitative insights into the turbulent flow structures that develop inside the channel and to study the effect of the mesh enlargement, large eddies have been depicted on Fig. 28 using the well known Q criterion for the PITM2 simulation. The value of the parameter $Q = \frac{1}{2}(\Omega_{ij}\Omega_{ij} - S_{ij}S_{ij})$ is defined as the balance between the local rotation rate $\boldsymbol{\Omega}$ and the strain rate $\boldsymbol{S}$ of the filtered velocity, in order to identify packets of flow vortices. As no differences were visible at a first sight between PITM2 and PITM3, the structures associated with PITM3 are not plotted here. This Fig. reveals the presence of very large longitudinal roll cells that develop in the entire channel illustrating the three dimensional nature of the flow. As expected, the fact to coarsen the grid-size ratio in the streamwise direction has the effect to modify the flow structures that become more elongated in this direction as the flow moves towards the exit section of the channel. One can see a drastic diminution of eddies computed on the coarse grid. Such qualitative results were also observed by Chaouat and Schiestel (2013) for the channel flow over periodic hills (see Fig. 3).

11 Concluding remarks

We have analytically derived the complex expressions of the commutation terms appearing in the filtered turbulence equations using the rules of convolution operators with variable kernels. In this framework, we have developed a mathematical physics formalism for integrating the commutation terms in the PITM method and given its physical interpretation in the spectral space. These terms were computed by means of a superfilter which was applied on the filtered equation of mass, momentum and turbulence. The application of the fully turbulent channel flow was considered for illustrating the role of the commutation errors in PITM simulations. In particular, simulations have been performed on several grids including a sudden grid step increase in the grid-size in the streamwise direction by means of a numerical tool that is free from any contamination errors from the inlet condition. As a result, it has been found that PITM2 accounting for the commutation terms and PITM3 return quite similar results even if a slight improvement in the development of the subfilter stresses is however obtained for PITM2, relatively to PITM3. The subfilter scale energy increases as the grid-size increases since larger scales must be modeled and vice versa, the resolved scale energy decreases as the grid-size increases since less scales are simulated. But the total turbulent energy remains almost constant, the subfilter and resolved scales energies are just compensating from each other. In conclusion, it has been found that the impact of the commutation terms on the flow solution remains moderate even if the grid-size variation is increasing up to 400 % in the streamwise direction, but it has however a slight beneficial effect on the solution. This outcome of this work should be confirmed by other various extensive applications.

A Low Reynolds number formulation of the subfilter scale model

The present subgrid stress PITM model based on the transport equations (27) and (38) is used in a low Reynolds number formulation for approaching walls. The coefficients used in equation (41) are $\alpha = 3$ and $\gamma = 2/9$. The values of the coefficients used in the model are $c_{\epsilon_1} = 1.5$ and $c_{\epsilon_2} = 1.9$, respectively. The coefficient c_{ϵ_1} comes naturally in analytical developments performed in the spectral space (Chaouat and Schiestel, 2012). The constants values used in the diffusion terms in equations (32) and (39) are $c_s = 0.22$ and are $c_\epsilon = 0.18$, respectively. The coefficients c_1 and c_2 appearing in equations (30) and (31) depend on the Reynolds number and on the anisotropy tensor $(a_{ij})_{sfs} = [(\tau_{ij})_{sfs} - \frac{2}{3}k_{sfs}\delta_{ij}]/k_{sfs}$, the subfilter-scale invariants $A_2 = (a_{ij})_{sfs}(a_{ji})_{sfs}$, $A_3 = (a_{ij})_{sfs}(a_{jk})_{sfs}(a_{ki})_{sfs}$ and the flatness parameter $A = 1 - \frac{9}{8}(A_2 - A_3)$. For confined flows, a wall reflection term Π^3_{ij} accounting for the wall effects caused by the reflection of the pressure fluctuations from rigid walls is added in the redistribution term as follows

$$\begin{aligned} \Pi^3_{ij} &= c_{1w}\frac{\epsilon_{sfs}}{k_{sfs}}\left((\tau_{kl})_{sfs}n_k n_l\delta_{ij} - \tfrac{3}{2}(\tau_{ki})_{sfs}n_k n_j - \tfrac{3}{2}(\tau_{kj})_{sfs}n_k n_i\right) f_w \\ &+ c_{2w}\left(\Pi^2_{kl}n_k n_l\delta_{ij} - \tfrac{3}{2}\Pi^2_{ik}n_k n_j - \tfrac{3}{2}\Pi^2_{jk}n_k n_i\right) f_w \end{aligned} \tag{87}$$

The quantity n_i is the unit vector perpendicular to the wall, f_w is a near wall damping function, c_{1w} and c_{2w} are some functions calibrated to recover the logarithmic law of the velocity in the boundary layer. These functions used in the subgrid-scale model stress at low Reynolds number are listed in table (1). The coefficients $\alpha_1 = 1.4/400$ and $\alpha_2 = 1/400$.

Functions	Expressions
R_t	$k^2_{sfs}/(\nu\epsilon_{sfs})$
c_1	$\left([1 + 2.30\, A\, A_2^{1/8}\, [1 - \exp(-(R_t/140)^2)]\right) \alpha(\eta)$
c_2	$0.60A^{1/2}(1 - \exp(-\sqrt{R_t}))$
c_{1w}	$-\frac{2}{3}c_1 + \frac{5}{3}$
c_{2w}	$\max(\frac{2}{3}c_2 - \frac{1}{6}, 0)/c_2$
f_w	$\min(0.4k^{3/2}_{sfs}/(\epsilon_{sfs}x_n), 2.50)$
α	$(1 + \alpha_1\eta_c^2)/(1 + \alpha_2\eta_c^2)$

Table 1: Functions used in the subfilter stress model.

References

[1] Argyropoulos, C.D., Markatos, N.C., 2015. Recent advances on the numerical modelling of turbulent flows. Applied Math. Modelling 39, 693-732.

[2] Befeno, I., Schiestel, R., 2007. Non-equilibrium mixing of turbulence scales using a continuous hybrid RANS/LES approach: Application to the shearless mixing layer Flow, Turbul. Combust. 78, 129-151.

[3] Cambon, C., Jeandel, D., Mathieu, J., 1981. Spectral modelling of homogeneous non-isotropic turbulence. J. Fluid Mech. 104, 247-262.

[4] Chaouat, B., Schiestel, R., 2005. A new partially integrated transport model for subgrid-scale stresses and dissipation rate for turbulent developing flows. Phys. Fluids 17, 065106, 1-19.

[5] Chaouat, B., 2006. Reynolds stress transport modeling for high-lift airfoil flows. AIAA J. 44 (10), 2390-2403.

[6] Chaouat B., Schiestel, R., 2007. From single-scale turbulence models to multiple-scale and subgrid-scale models by Fourier transform. Theoret. Comput. Fluid Dyn. 21, pp 201-229.

[7] Chaouat, B., Schiestel, R., 2009. Progress in subgrid-scale transport modelling for continuous hybrid non-zonal RANS/LES simulations. Int. J. Heat Fluid Flow 30, 602-616.

[8] Chaouat, B., 2010. Subfilter scale transport model for hybrid RANS/LES simulations applied to a complex bounded flow. J. Turbul., 11 (51), 1-30.

[9] Chaouat, B., 2011. An efficient numerical method for RANS/LES turbulent simulations using subfilter scale stress transport equations. Int. J. Numer. Methods Fluids 67, 1207-1233.

[10] Chaouat, B., 2012. Simulation of turbulent rotating flows using a subfilter scale stress model derived from the partially integrated transport modeling method. Phys. Fluids 24, 045108, 1-35.

[11] Chaouat, B., Schiestel, R., 2012. Analytical insights into the partially integrated transport modeling method for hybrid Reynolds averaged Navier-Stokes equations-large eddy simulations of turbulent flows. Phys. Fluids 24, 085106, 1-34.

[12] Chaouat, B., Schiestel, R., 2013. Hybrid RANS-LES simulations of the turbulent flow over periodic hills at high Reynolds number using the PITM method. Comput. Fluids, 84, 279-300.

[13] Chaouat, B., Schiestel, R., 2013. Partially integrated transport modeling method for turbulence simulation with variable filters. Phys. Fluids 25, 125102, 1-39.

[14] Chaouat, B., 2017a. The state of the art of hybrid RANS/LES modeling for the simulation of turbulent flows. Flow, Turbul. Combust. 99, 279-327.

[15] Chaouat, B., 2017b. Application of the PITM method using inlet synthetic turbulence generation for the simulation of the turbulent flow in a small axisymmetric contraction. Flow, Turbul. Combust. 98, 987-1024.

[16] Fröhlich, J., Denev, J.A, Hinterberger, C., Bockhorn, H., 2007. On the impact of tangential grid refinement on subgrid-scale modelling in large eddy simulation. in 6th International Conference on Numerical Method and Applications (NMA), Ed. by Boyanov T., Dimova, S., Georgiev K. and Nikolov G., Springer, pp. 550-557.

[17] Fröhlich J., Von Terzi, D., 2008. Hybrid LES/RANS methods for the simulation of turbulent flows. Prog. Aerosp. Sci. 44, 349-377.

[18] Fureby, C., Tabor, G., 1997. Mathematical and physical constraints on large-eddy simulations. Theoret. Comput. Fluid Dyn. 9, 85-102.

[19] Gatski, T.B., Rumsey, C.L., Manceau, R., 2007. Current trends in modelling research for turbulent aerodynamic flows. Philos. Trans. R. Soc. London, Ser. A 365, 2389-2418.

[20] Geurts, B.J., van der Bos, F., 2005. Numerically induced high-pass dynamics in large-eddy simulation. Phys. Fluids 17, 125103, 1-12.

[21] Geurts, B.J., Holm, D.H., 2006. Commutator errors in large eddy simulation. J. Phys. A: Math. Gen. 39, doi:10.1088/0305-4470/39/9/015.

[22] Ghosal, S., Moin, P., 1995. The basic equations for large eddy simulation of turbulent flows in complex geometries. J. Comput. Phys. 118, 24-37.

[23] Hamba, F., 2009. Log-layer mismatch and commutation error in hybrid RANS/LES simulation of channel flow. Int. J. Heat Fluid Flow 30, 20-31.

[24] Hamba, F., 2011. Analysis of filtered Navier-Stokes equation for hybrid RANS/LES simulation. Phys. Fluids 23, 015108, 1-13.

[25] Hanjalic, K., Launder, B.E, 2011. Modelling turbulence in engineering and the environnement. Second-moment route to closure, Cambridge University Press.

[26] Iovieno, M., Tordella D., 2003. Variable scale filtered Navier-Stokes equations: A new procedure to deal with the associated commutation error. Phys. Fluids 15, 7, 1926-1936.

[27] Jakirlic, S., Maduta, R., 2015. Extending the bounds of steady RANS closures: Toward an instability-sensitive Reynolds stress model. Int. J. Heat Fluid Flow 51, 175-194.

[28] Kenjeres, S., de Wildt, S., Busking, T., 2015. Capturing transient effects in turbulent flows over complex urban areas with passive pollutants. Int. J. Heat Fluid Flow 51, 120-137.

[29] Lesieur, M., Metais O., 1996. New trends in large-eddy simulations of turbulence. Ann. Rev J. Fluid Mech. 28, 45, 45-82.

[30] Lumley, J.L., 1978. Computational Modeling of Turbulent Flows. Advances Applied Mech. 18, 123-176.

[31] Moser, R., Kim, D., Mansour, N., 1999. Direct numerical simulation of turbulent channel flow up to $R_\tau = 590$. Phys. Fluids 11, 943-945.

[32] Schiestel, R., Dejoan, A., 2005. Towards a new partially integrated transport model for coarse grid and unsteady turbulent flow simulations. Theoret. Comput. Fluid Dyn. 18, 443-468.

[33] Schiestel, R., 1987. Multiple-time scale modeling of turbulent flows in one point closures. Phys. Fluids 30, 722-731.

[34] Schiestel, R., 2008. Modeling and simulation of turbulent flows. ISTE Ltd and J. Wiley.

[35] Schumann, U. 1977. Realizability of Reynolds Stress Turbulence Models. Phys. Fluids 20, (5), 721-725.

[36] Speziale, C.G., Abid, R., Durbin, P.A., 1994. On the Realisability of Reynolds Stress Turbulence Closures. J. Scientific Comput. 9, (4), 369-403.

[37] Stoellinger, M., Roy, R., Heinz, S., 2015. Unified RANS-LES method based on second-order closure. In Proceedings of the 9th Symposium on Turbulence Shear Flow Phenomena, 7B5, pp. 1-6.

[38] van des Bos, F., Geurts, B.J., 2004. Dynamic of commutator-errors in LES with non-uniform filter width. Direct and Large Eddy Simulation V, ERCOFTAC Vol. 9 edited by R. Friedrich, B. J. Geurts and O. Métais, (Kluwer Academic), 155-162.

[39] van der Bos, F., Geurts, B.J., 2005. Commutator errors in the filtering approach to large-eddy simulation. Phys. Fluids 17, 035108, 1-20.

[40] Vasilyev, O.V., Lund, T.S., Moin, P. (1998). A general class of commutative filters for LES in complex geometries. J. Comput. Phys. 146, 82-104.

[41] Vichnevetsky, R., 1982. Fourier analysis of numerical approximation of hyperbolic equations. SIAM, Philadelphia.

[42] Vreman, B., Geurts, B.J., Kuerten, H., 1994. Realizability conditions for the turbulent stress tensor in large eddy simulation. J. Fluid Mech. 278, 351-362.